Grain size reduction by plug flow in the wet oceanic upper mantle explains the asthenosphere's low seismic Q zone

Florence Ramirez[1], Clinton P. Conrad[1], and Kate Selway[2]

[1]University of Oslo
[2]University of South Australia

November 21, 2022

Abstract

The prominent seismic low-velocity zone (LVZ) in the oceanic low-viscosity asthenosphere is approximately coincident with a zone of high seismic attenuation (or low seismic Q). Small grain sizes in the asthenosphere could link these seismic and rheological properties as small grain sizes reduce viscosity and also lower seismic velocity and seismic Q. Because grain-size is reduced by rock deformation, the asthenosphere's seismic properties can place constraints on asthenospheric deformation or flow. To determine dominant flow patterns, we develop a selfconsistent analytical 1-D channel flow model that accounts for upper mantle rheology and its dependence on flow-modified grain-sizes, water content and melt fraction, both for flow driven by surface plate motions (Couette flow) and/or by horizontal pressure gradients (Poiseuille flow). From our flow models, Couette flow dominates if the upper mantle is dry, and plug flow (a Poiseuille flow for power law rheology) if it is wet. A plug flow configuration spanning the upper 670 km of the mantle best explains the low seismic Q zone in the asthenosphere, which can be attributed to significant grain-size reduction due to extensive shearing across the asthenosphere. Below the asthenosphere, high water content and minimal shear deformation promote large grain sizes and high seismic Q. We suggest that asthenospheric low-Q and LVZ can be largely explained by grain-size variations associated with plug flow in the wet upper mantle.

Grain size reduction by plug flow in the wet oceanic upper mantle explains the asthenosphere's low seismic Q zone

Florence D. C. Ramirez[1,2,*], Clinton P. Conrad[1] and Kate Selway[1,3]

[1] Centre for Earth Evolution and Dynamics, University of Oslo, Norway

[2] Department of Earth and Environmental Sciences, Macquarie University, Australia

[3] Future Industries Institute, University of South Australia

Abstract

The prominent seismic low-velocity zone (LVZ) in the oceanic low-viscosity asthenosphere is approximately coincident with a zone of high seismic attenuation (or low seismic Q). Small grain sizes in the asthenosphere could link these seismic and rheological properties as small grain sizes reduce viscosity and also lower seismic velocity and seismic Q. Because grain-size is reduced by rock deformation, the asthenosphere's seismic properties can place constraints on asthenospheric deformation or flow. To determine dominant flow patterns, we develop a self-consistent analytical 1-D channel flow model that accounts for upper mantle rheology and its dependence on flow-modified grain-sizes, water content and melt fraction, both for flow driven by surface plate motions (Couette flow) and/or by horizontal pressure gradients (Poiseuille flow). From our flow models, Couette flow dominates if the upper mantle is dry, and plug flow (a Poiseuille flow for power law rheology) if it is wet. A plug flow configuration spanning the upper 670 km of the mantle best explains the low seismic Q zone in the asthenosphere, which can be attributed to significant grain-size reduction due to extensive shearing across the asthenosphere. Below the asthenosphere, high water content and minimal shear deformation promote large grain sizes and high seismic Q. We suggest that asthenospheric low-Q and LVZ can be largely explained by grain-size variations associated with plug flow in the wet upper mantle.

Keywords: Poiseuille flow, low seismic Q, seismic low-velocity zone, mantle water content, grain-size variations, asthenospheric plug flow

[*] Corresponding author at: Centre for Earth Evolution and Dynamics (CEED), University of Oslo, Sem Sælands vei 2A, 0371 Oslo, Norway
Email address: f.d.c.ramirez@geo.uio.no

1. Introduction

A seismic low-velocity zone (LVZ; Figure 1) between $\sim 100 - 250$ km depth is a prominent feature below the oceanic lithosphere that is consistently reported by global and local seismological models (e.g., Dalton et al., 2009). Since the LVZ was discovered by Gutenberg (1959), researchers have noted its overlap with the asthenosphere (Figure 1), the low-viscosity zone that facilitates mantle deformation beneath the tectonic plates (e.g., Richards et al., 2001). Indeed, the deformation of asthenospheric rocks is illuminated by a seismically-anisotropic layer (high anisotropy zone, Figure 1; e.g., Nettles and Dziewonski, 2008) that is produced by shear deformation of olivine (e.g., Tommasi et al., 1999; Jung and Karato, 2001). This deformation drives grain-size reduction (e.g., Behn et al., 2009), which can decrease both the seismic velocity (e.g., Faul and Jackson, 2005) and the effective mantle viscosity (e.g., Warren and Hirth, 2006; Hirth and Kohlstedt, 2003), potentially amplifying the deformation. Stiff plates may also trap partial melt (e.g., Chantel et al., 2016; Selway and O'Donnell, 2019; Debayle et al. 2020), reducing seismic velocities.

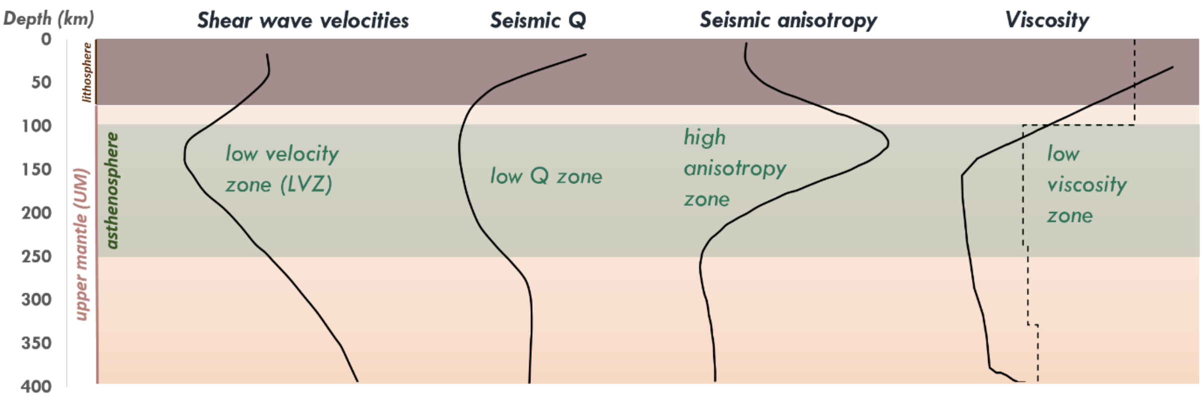

Figure 1. Schematic representation of seismic observations and inferred viscosities in the oceanic upper mantle (above 400 km) where low velocity, low Q, high radial anisotropy, and low viscosity zones exist within the same approximate depth range (the asthenosphere, green region). The shear wave velocity model shown is from Nettles and Dziewonski (2008) for 25-100 Myr oceanic plate ages, the global seismic Q factor is from Karaoglu and Romanowicz (2018), and the global seismic radial anisotropy is from Nettles and Dziewonski (2008) for mid-age oceans. The viscosity profiles are inferred from mantle flow models where the solid line is for purely temperature-dependent viscosity (Becker, 2006), and the dashed line is geoid-constrained viscosity (Steinberger and Calderwood, 2006).

In addition to reducing seismic wave speeds, both grain-size reduction and partial melt dissipate seismic energy, and indeed the LVZ is approximately coincident with a zone of high seismic attenuation (low seismic Q zone, Figure 1). The LVZ, the low-Q zone, and low viscosity asthenosphere all overlap (Figure 1), and the coincident layer of seismic anisotropy suggests that all three are linked together with asthenospheric deformation. Grain-size reduction, which is driven by rock deformation, is an obvious explanation, because it reduces seismic velocity, seismic Q, and effective viscosity. Indeed, without grain-size variations produced by asthenospheric deformation, the forward-prediction of seismic structures (Figure S1) does not reproduce the low Q zone in the asthenosphere, and the amplitude of the LVZ is underpredicted. The patterns of rock deformation in the asthenosphere exert an important control on upper mantle seismic properties, and indeed we can use seismic observations of the LVZ and low-Q zone to constrain models of asthenospheric deformation.

Using grain size evolution models (e.g., Austin and Evans, 2007; Hall and Parmentier, 2003), we investigate time-dependent depth variations of grain size resulting from flow-induced deformation within the upper mantle. Behn et al. (2009) already showed the importance of grain size evolution for the seismic structures associated with asthenospheric shear (Couette flow, Figure 2a), but recent studies have suggested that pressure-driven (Poiseuille, Figure 2b) flow may be the dominant mode of deformation within much of the upper mantle (e.g., Höink and Lenardic, 2010; Semple and Lenardic, 2018). Couette flow arises due to the motion of a surface plate that shears the asthenosphere below it in a linear fashion, while Poiseuille flow is induced by pressure gradients across the upper mantle associated with mantle upwellings and downwellings and/or lateral density variations. By developing an analytical model that incorporates realistic upper mantle flow configurations (combined Couette and Poiseuille flows), we determine how grain-size variations depend on flow drivers such as plate speed and horizontal pressure gradient, and on mantle parameters such as water content and melt fraction.

Although water content (e.g., Karato and Jung, 1998; Karato 2012) does not significantly affect seismic attenuation (Cline et al. 2018), it does affect viscosity (e.g., Mei and Kohlstedt, 2000; Hirth and Kohlstedt, 2003). We also investigate feedbacks between grain-size, asthenosphere flow, rheology, and deformation mechanism. From the modelled flow in the upper mantle, we make predictions of seismic structures that can be tested against observations of seismic velocity and attenuation in the upper mantle. This comparison places constraints on mantle conditions and dominant flow types necessary to explain the observed LVZ and low Q zone.

2. Types of flow in the oceanic upper mantle

Several analytical and numerical studies show that flow in the upper mantle results from a combination of Couette (plate-driven, Figure 2a) and Poiseuille (pressure-driven, Figure 2b) flows (e.g., Lenardic et al., 2006; Höink and Lenardic, 2010; Natarov and Conrad, 2012). If Couette flow occurs via dislocation creep, this shearing flow produces a lattice-preferred orientation of olivine crystals that form a single seismically anisotropic layer (Figure 2a). Two distinct anisotropic layers, as detected by Lin et al. (2016) at the top and the base of the asthenosphere, can be formed by separate shear zones if the asthenosphere additionally hosts Poisuille flow (Figure 2b). If the upper mantle has a Newtonian rheology, a Newtonian Poiseuille flow (termed *PFn1* here, where *'n1'* denotes the stress exponent $n=1$, Figure 2b.1) is produced. For a power-law rheology, the flow is dominated by the so-called "plug flow" (termed *PFn3* here, for $n=3$, Figure 2b.2), with approximately uniform velocity in the middle of the low-viscosity layer, bounded above and below by zones of intense shear deformation (Semple and Lenardic, 2018).

3. Analytical plate- and pressure-driven flow model for the oceanic upper mantle

We develop an analytical 1-D channel flow model (Sections 3.1 and 3.2) for the oceanic mantle to investigate the effect of flow configurations on rheology (Section 4) and seismic structures

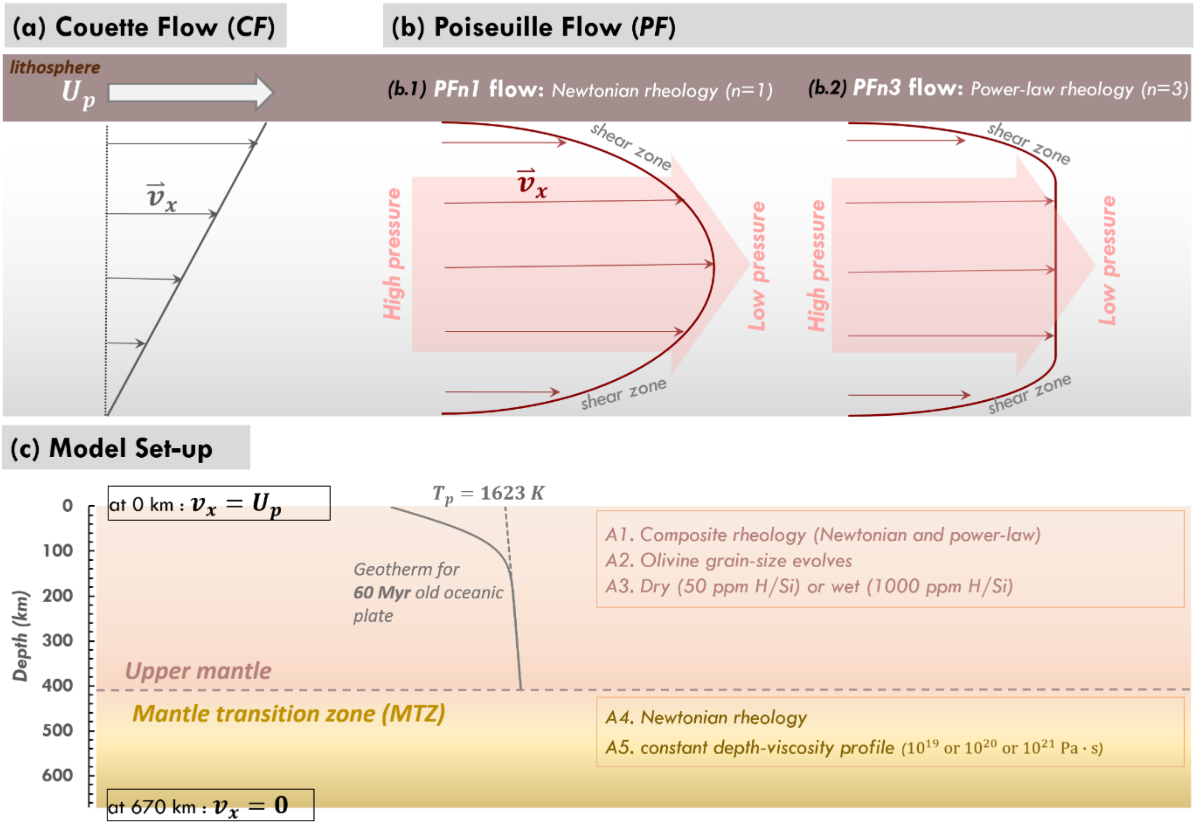

Figure 2. (a-b) Dominant flow regimes in the upper mantle: Sketch of flow velocities ($\vec{v}_x$) due to (a) Couette flow (CF) driven by surface plate motion and (b) Poiseuille flow (PF) driven by a lateral pressure gradient. The rheology of the upper mantle determines the PF flow configuration, where (b.1) a parabolic-shaped velocity profile arises if the rheology is Newtonian (termed PFn1 here), or (b.2) a plug flow arises for power-law rheology (termed PFn3 here). **(c) Model set-up.** We consider a 60 Myr old oceanic plate with 1623 K potential temperature (T_p) that results in a temperature profile shown in (c). We assume that the oceanic upper mantle (defined here as the region above 410 km) is governed by a composite olivine rheology, which is controlled by the geotherm, grain sizes and water content (dry or wet). We also consider the mantle transition zone (MTZ, 410 – 670 km) in our analytical model to investigate its effect on the flow configurations of the upper mantle flow region above it. Since the rheology of the MTZ is not well constrained by experiments, we assumed that it has a Newtonian rheology and a constant viscosity. With the calculated (above 410 km) and assigned (for the MTZ) rheologies, the flow velocities are calculated using Eqs. (6.2) and (A.5), where the boundary conditions are shown in (c).

(Section 5), particularly in the seismically anomalous and weak asthenosphere. We let the rheology of the mantle determine the style of flow and the associated flow rates and stresses (Section 3.2). At the same time, the flow alters the olivine grain size with time until the size stabilizes (Section 3.3) by utilizing the available grain size evolution models (e.g., Austin and Evans, 2007; Hall and Parmentier, 2003). Thus, the temporal evolution of olivine grain size requires us to also calculate the time-evolution of the shear stresses, horizontal velocities and viscosities (Section 3.4). From this, we can account for possible feedbacks between flow configurations, rheology, deformation, and grain-size.

3.1 Model Set-up

Since we do not know the appropriate depth and the velocity boundary condition at the base of the asthenosphere (green region, Figure 1), we incorporate the entire oceanic mantle down to 670 km (including lithosphere, asthenosphere, upper mantle, and mantle transition zone; Figure 2c) into our model. We impose a plate speed U_p at 0 km to drive Couette flow (Figure 2a), and a zero flow condition ($v_x = 0$) at 670 km, which assumes that flow is much slower in the highly viscous lower mantle. We assign a lateral pressure gradient (dp/dx) across the layers above 670 km to drive Poiseuille flow (Figure 2b). From the U_p and dp/dx drivers, the resulting flow configuration and the associated flow velocities (v_x) are determined by the composite rheology above 410 km, and the assigned Newtonian rheology of the mantle transition zone (Section 3.2). The rheology above 410 km is dictated by the assigned water content (50 ppm H/Si or 1000 ppm H/Si) and melt fraction, the computed geotherm for a 60 Myr oceanic plate with 1623 K potential temperature (Figure 2c; using Equation (4.113) of Turcotte and Schubert (2014)), and the deformation-dependent olivine grain size. This results in a cold and highly viscous lithosphere at depths shallower than ~100 km and a deformable upper mantle layer between the lithosphere and the mantle transition zone. Although the mantle transition zone (410 – 670 km) may deform under dislocation creep (e.g., Ritterbex et al., 2020), we assigned a Newtonian viscosity in the range $10^{19} - 10^{21}$ Pa·s (e.g., Kaufmann and Lambeck, 2000; Forte and Mitrovica, 1996) because the flow laws for ringwoodite and wadsleyite (polymorphs of olivine that are stable in the mantle transition zone) are not well constrained by experiments.

3.2 Working equations for the 1D flow model

Both plate- and pressure-driven flows are governed by the Navier-Stokes equation.

$$\rho \frac{D\vec{V}}{Dt} = -\nabla p + \vec{F} + \eta \nabla^2 \vec{V} \tag{1}$$

When neglecting the inertial term $\frac{D\vec{V}}{Dt}$ and body forces $\vec{F}$, we are left with pressure and viscous terms for a 1D model,

$$-\frac{\partial p}{\partial x} + \frac{\partial}{\partial z}\left(\eta(z)\frac{\partial v_x}{\partial z}\right) = 0 \tag{2.1}$$

$$-\frac{\partial p}{\partial x} + \frac{\partial}{\partial z}(\tau_{xz}) = 0 \tag{2.2}$$

where $\frac{\partial p}{\partial x}$ is a constant horizontal pressure gradient, $\eta(z)$ is depth-dependent viscosity, τ_{xz} is the shear stress, and v_x is the horizontal velocity (either plate-driven or pressure-driven). Integrating Equation (2.2) with respect to z yields an estimate of the shear stress $\tau_{xz} = \tau$ induced by the flow at every layer i of our 1D model as described by

$$\tau_i = \frac{\partial p}{\partial x} z_i \; + \; C_i \tag{3}$$

where C_i is a constant of integration.

When assuming a composite rheology (that is, rheology controlled by both diffusion and dislocation creep), the total strain rate (Hirth and Kohlstedt, 1996) per layer is

$$\dot{\varepsilon}_{total,i} = \dot{\varepsilon}_{diff,i} + \dot{\varepsilon}_{disl,i} = \frac{\sigma}{\eta_{eff,i}} \tag{4}$$

where $\dot{\varepsilon}_{diff}$ is the strain rate for diffusion creep, $\dot{\varepsilon}_{disl}$ is the strain rate for dislocation creep, η_{eff} is the effective viscosity, and σ is the differential stress which is equivalent to 2τ. We assume that *PFn1* dominates for the diffusion creep regime (*n*=1) as predicted by Höink et al. (2011) and *PFn3* dominates for dislocation creep regime (*n*=3) as illustrated by Semple and Lenardic (2018).

The strain-rate components are defined according to their relevant rheological relationships,

$$\dot{\varepsilon}_{diff,i} = A_{PFn1,i}\tau_i = \frac{\partial v_{PFn1,i}}{\partial z} \tag{5.1}$$

$$\dot{\varepsilon}_{disl,i} = A_{PFn3,i}{\tau_i}^3 = \frac{\partial v_{PFn3,i}}{\partial z} \tag{5.2}$$

$$A_{PFn1,i} = A_{diff}{C_{OH}}^{r_{diff}} d^{-p_{diff}} \exp(\propto_{diff}\varphi) \exp\left[-\frac{E_{diff}+PV_{diff}}{RT}\right] \tag{5.3}$$

$$A_{PFn3,i} = A_{disl}{C_{OH}}^{r_{disl}} d^{-p_{disl}} \exp(\propto_{disl}\varphi) \exp\left[-\frac{E_{disl}+PV_{disl}}{RT}\right] \tag{5.4}$$

by applying the empirically determined flow laws (Hirth and Kohlstedt, 2003). The $v_{PFn1,i}$ and $v_{PFn3,i}$ in Equations (5.1) and (5.2) are the horizontal velocities for *PFn1* and *PFn3* flow configurations, respectively. The parameters for the upper mantle defined in Equations (5.3) and (5.4) prescribe the rheological impact of grain-size d, water content C_{OH}, and melt fraction φ (other parameters are defined in Table S1; Supplementary Information). For the mantle transition zone with an assigned Newtonian rheology ($\dot{\varepsilon}_{total} = \dot{\varepsilon}_{diff}$ and $\eta_{eff} = \eta_{MTZ}$ where η_{MTZ} is the assigned viscosity), the parameters are $A_{PFn1,i} = 2/\eta_{MTZ}$ derived by combining Equations (5.1) and (4), and $A_{PFn3,i} = 0$.

The overall $v_{x,i}$ is $v_{PFn1,i} + v_{PFn3,i}$, where the velocity components are integrals of Equations (5.1) and (5.2) with respect to z, respectively:

$$v_{x,i} = \int A_{PFn1,i}\tau_i dz + \int A_{PFn3,i}{\tau_i}^3 dz \tag{6.1}$$

Substituting the τ_i in Equation (6.1) with Equation (3), and then integrating them with respect to z yields:

$$v_{x,i} = A_{PFn1,i}\left[\frac{1}{2}\frac{\partial p}{\partial x}{z_i}^2 + C_i z_i\right] + A_{PFn3,i}\begin{bmatrix}\frac{1}{4}\left(\frac{\partial p}{\partial x}\right)^3 {z_i}^4 + C_i\left(\frac{\partial p}{\partial x}\right)^2 {z_i}^3 \\ +\frac{3}{2}{C_i}^2\frac{\partial p}{\partial x}{z_i}^2 + {C_i}^3 z_i\end{bmatrix} + k_i \tag{6.2}$$

where k_i is the constant of integration and the involved parameters are summarized in Table S1 (Supplementary Information). When $\frac{\partial p}{\partial x} = 0$, Equations (3) and (6.2) describe a Couette flow configuration.

Implementing the necessary boundary conditions and linearizing the problem as described in Supplementary Information B, we estimate the horizontal velocity (Equation 6.2) and shear stress (Equation 3) structures.

3.3 Olivine grain size evolution model for the upper mantle

During deformation, mineral grains in mantle rocks temporally evolve to a stable size for which the grain growth rate equilibrates with the grain reduction rate. We mainly employ the grain-size evolution model of Austin and Evans (2007),

$$\textit{AE07 model}: \quad \dot{d} = {p_g}^{-1} d^{1-p_g} G_o \exp\left(-\frac{E_g+PV_g}{RT}\right) - \chi c^{-1} \gamma^{-1} \sigma \dot{\varepsilon}_{disl} d^2 \qquad (7)$$

where the first term describes the grain growth rate $\dot{d}_{gg}$, and the second term describes dynamic recrystallization rate $\dot{d}_{dr}$ that results in grain size reduction. The parameter values used in this study are summarized in Table S1 (Supplementary Information). When there is no mechanical work or deformation (i.e., $\dot{\varepsilon}_{disl} = 0$), the total grain size evolution is equivalent to the grain growth rate (first term, Equation 7). When deformation does occur, new grain boundaries may be created (second term > 0), which results in grain size reduction. Because larger grains are subdivided faster than smaller grains, the rate of grain size reduction (second term, Equation 7) increases with grain size. At depths with minimum stress, water promotes grain growth through significant reduction in $\dot{\varepsilon}_{disl}$ (first term > second term, Equation 7).

3.4 Temporal evolution of olivine grain-size, rheology and flow configuration

Using the detailed set-up described above and in Supplementary Information B, C and D, we investigate how the flow configuration, shear stress, rheology, and deformation evolve with

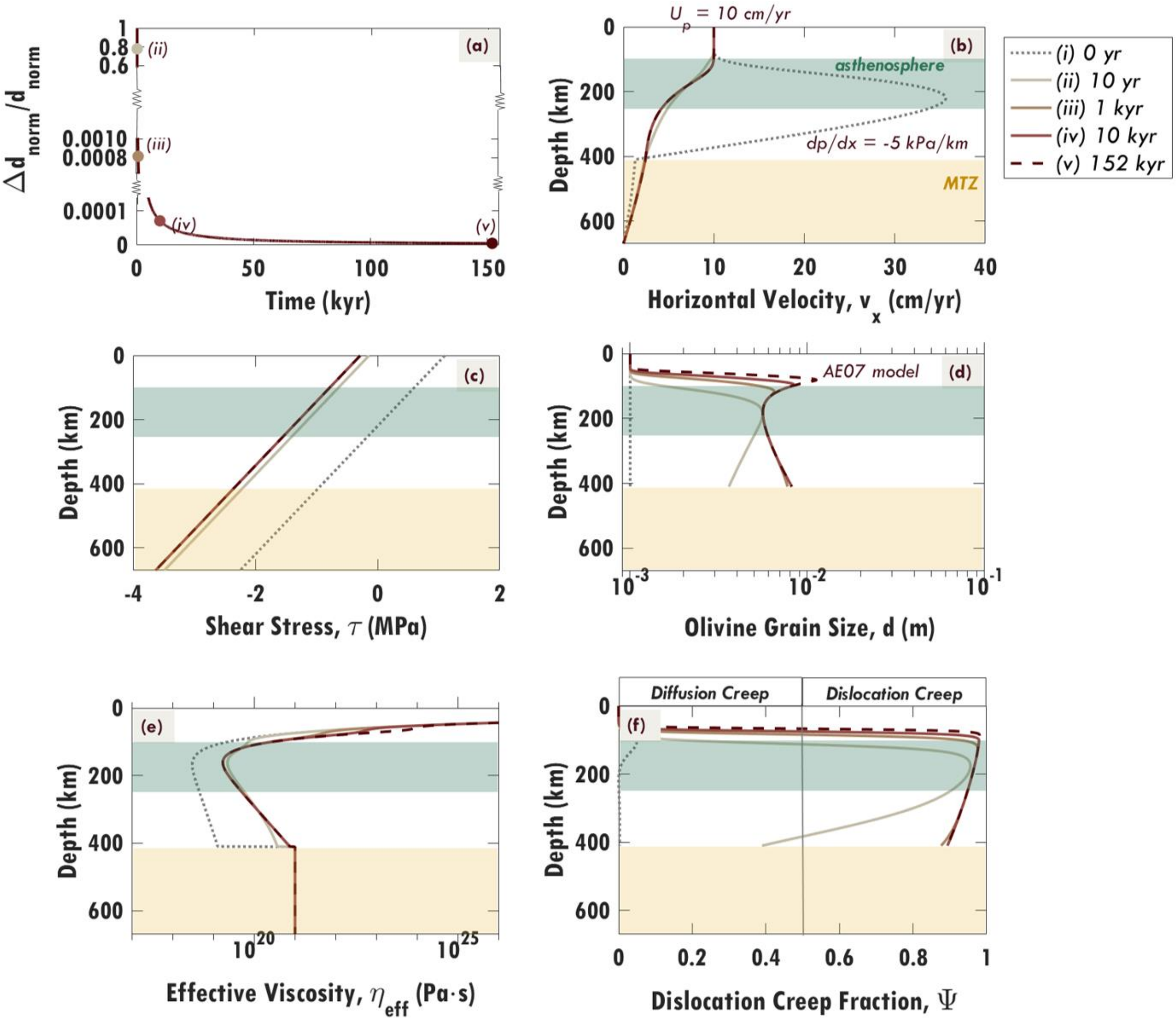

Figure 3. Temporal evolution of flow with an imposed pressure gradient (-5 kPa/km) and plate velocity (10 cm/yr). The upper mantle (above 410 km) is dry (50 ppm H/Si) and has an initial (at 0 yr) constant (10^{-3} m or 1 mm) olivine grain-size. The mantle transition zone (MTZ, yellow region, 410-670 km) with a viscosity of 10^{21} $Pa \cdot s$ is assumed to deform together with the upper mantle. During the deformation induced by the flow (b), olivine grain-sizes evolve (d) following the AE07 model (Austin and Evans, 2007) as in Equation (7) until the grain-size structure stabilizes (in panel (a), which shows the time evolution of the convergence criterion ($\Delta d_{norm}/d_{norm}$ for timestep Δt = 10 yr; Supplementary Information D)) after 152 kyr. Consequently, the flow configuration (b), shear stress profiles (c), effective viscosity (e) and the deformation type (f) evolve and stabilize. The initially PFn1 flow (dotted line) becomes dominantly Couette flow because the increased grain-size (d) leads to a greater upper mantle viscosity (e). The green region is the asthenosphere (100 -250 km), with a low viscosity zone (e).

time in the oceanic mantle (Figure 3). Here we consider a 10 cm/yr plate velocity and -5 kPa/km pressure gradient across the dry (50 ppm H/Si) upper mantle and a 10^{21} Pa·s mantle transition zone (MTZ). Initially (0 yr), we assume a constant grain-size of 1 mm that results in a *PFn1* flow (Figure 3b) because this small grain size induces low effective viscosity (Figure 3e). Given enough time, olivine grain-sizes evolve during the flow-driven deformation to a steady-state structure (Figure 3a and 3d). We find that steady state is reached after only 152 kyr (only 0.3% of the plate age), which is significantly quicker than mantle flow time scales. This indicates that the grain size is always in effective equilibrium for steady-state mantle flow problems, and that the adjustment associated with the grain-size evolution (Figure 3d) and the associated changes to the flow field (Figure 3b), stresses (Figure 3c), viscosity (Figure 3e) and deformation style (Figure 3f), can be considered essentially instantaneous.

Although the initial grain size does not affect the final grain size at steady state (Supplementary Information E.1), the choice of initial grain size does affect the time it takes the grain size to stabilize (Figure S3). A larger initial grain size (e.g., 10 mm) stabilizes faster than a smaller grain size (1 mm), because large grains subdivide more rapidly than small grains, which tend to grow before subdividing (Equation 7). In the following section, we assume an initial grain size of 10 mm because it reaches steady state faster, and thus reduces calculation time.

4. Link between flow configurations and rheologies of the oceanic upper mantle

Here, we investigate how water content, grain-size, the imposed plate velocity and the horizontal pressure gradient control the dominant flow configuration of the upper mantle (Figure 4). We consider dry (50 ppm H/Si) and wet (1000 ppm H/Si) conditions for layers above the mantle transition zone, and assign 10^{21} Pa·s for mantle transition zone viscosity if the upper mantle is dry and 10^{20} Pa·s if it is wet. This setup maintains comparable effective viscosities for the upper mantle and mantle transition zone layers, and we investigate flow configurations for contrasting rheologies later (Section 7). We vary the plate velocity between 0 and 10 cm/yr in the direction of pressure-driven flow, and horizontal pressure gradients between 0 and -5 kPa/km (e.g., Natarov and Conrad, 2012).

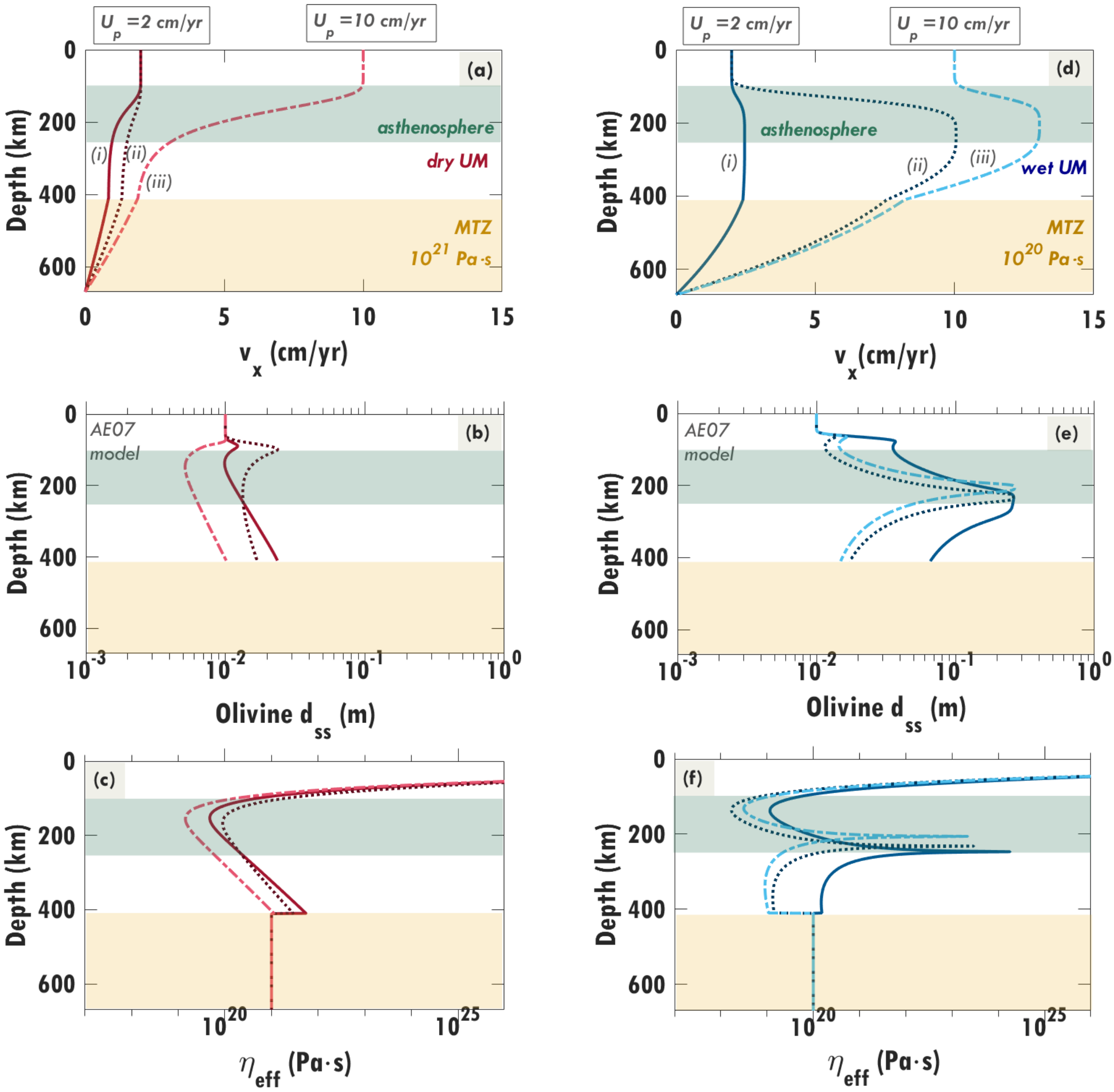

Figure 4. Factors affecting upper mantle flow (a, d), grain-size (b, e), and viscosity (c, f) at steady state for dry (a-c) and wet (d-f) conditions. Different combinations of imposed plate velocity and horizontal pressure gradient (labeled as i, ii and iii) are considered, where U_p and dp/dx are (i) 2 cm/yr and -1 kPa/km, (ii) 2 cm/yr and -3 kPa/km, and (iii) 10 cm/yr and -3 kPa/km. Dry upper mantle (50 ppm H/Si) flows via Couette flow (a) while wet upper mantle (1000 ppm H/Si) flows via PFn3 (d). Nonetheless, grain size reduction in the asthenosphere (b, e) results in a low viscosity zone (c, f). Grain growth at the bottom of the asthenosphere occurs only for PFn3 (e) because of very low flow-induced-stresses, and produces a peak in viscosity (f).

The water content of the upper mantle controls rheology both directly via weakening minerals and indirectly via grain-size evolution, and thus determines the type of flow. We find that if water is present in the upper mantle, *PFn3* is likely to dominate (Figure 4d). Otherwise, Couette flow dominates (Figure 4a) because the higher viscosities associated with a dry upper mantle do not permit Poiseuille flow. As a feedback mechanism, the flow configuration dictates the grain-size structure and thus also the viscosity structure. If the upper mantle is *PFn3*-dominated (Figure 4d), a viscosity peak (Figure 4f) develops, associated with very large grain-sizes (Figure 4e). Such large grain-sizes form in the mid-upper mantle because plug flow (*PFn3*) features approximately constant horizontal velocities, and deformation is therefore minimal and grain-size reduction is slow (Equation 7). Extensive shearing above and below the non-deforming region results in significant grain-size and viscosity reduction in both the shallow and deep upper mantle. In contrast, a Couette-flow-dominated upper mantle (Figure 4a), which is more typical of dry conditions, features grain-sizes that gradually increase with depth (Figure 4b) and is associated increasing effective viscosity (Figure 4c). Regardless of the flow configuration, the grain-size reduction due to shear deformation controls the low viscosity zone in the asthenosphere. In general, an increase in the magnitude of the horizontal pressure gradient increases the stress induced by pressure-driven flow, which eventually overwhelms plate-driven flow (case i vs. ii, Figure 4d). The resulting increase in stress produces smaller grain-sizes, which may make diffusion creep important ($\Psi < 1$). However, in our forward models, the grain sizes remain larger than ~ 3 mm (as in Figure 3d), which is large enough for dislocation creep to remain dominant.

5. Predicted seismic structures for dry and wet oceanic upper mantle

To quantify the impact of flow configurations on upper mantle seismic structure, we estimate the shear wave velocity V_S and seismic quality factor Q for the steady-state grain sizes associated with the different plate velocity and pressure-gradient combinations considered in Section 4. We estimate V_S (Figure 5b and 5d) following the formulation of Karato (1993), which is Q-dependent. We calculate the Q factor (Figure 5a and 5c) using the grain-size dependent formulation of Jackson and Faul (2010) at 100 s period, which is representative for seismic imaging of the upper mantle (e.g., Debayle, et al., 2020).

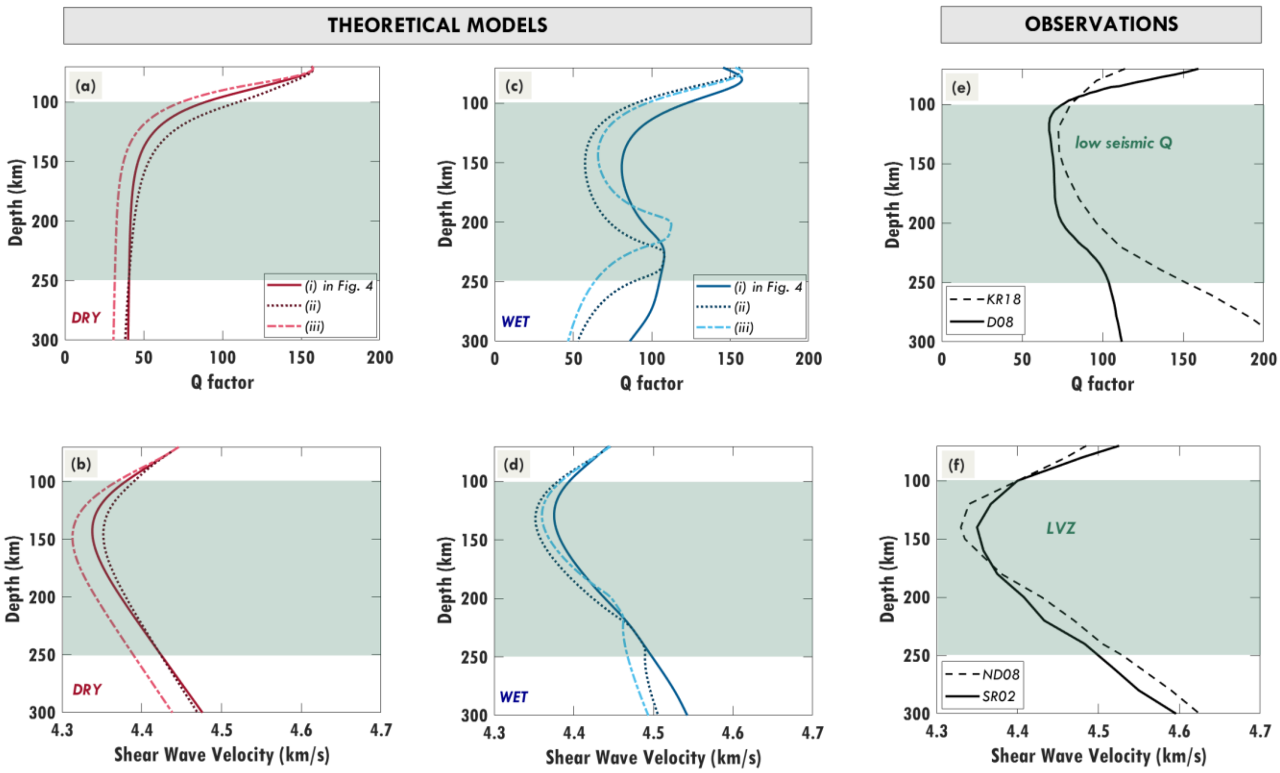

Figure 5. (a-d) Theoretical seismic models, computed for cases (i) to (iii) from Figure 4. The theoretical Q values for dry (a) and wet (c) conditions are calculated using the steady-state grain sizes in Figure 4b and 4e, as are the theoretical shear wave velocity profiles (b and d). **(e) Observations of Seismic Q** for comparison are the KR18 global Q model of Karaoglu and Romanowicz (2018) and the D08 model of Dalton et al. (2008) for mid-age oceans. **(f) Seismic velocity models** for comparison are the ND08 velocity model of Nettles and Dziewonski (2008) for 25-100 Myr old oceanic plate ages and SR02 model of Shapiro and Ritzwoller (2002) for 75 Myr age. The green region indicates the seismically anomalous asthenosphere (100-250 km depth) identified in Figure 1. All theoretical models except for Q within a dry upper mantle (panel (a)) show negative anomalies in the asthenosphere.

5.1 Effect of water content and flow configuration on seismic structures

Different grain size structures for dry (Figure 4b) and wet (Figure 4e) conditions result in different profiles for seismic Q (Figure 5a and 5c) and shear wave speeds (Figure 5b and 5d). Thus, water content indirectly, but significantly, impacts seismic signatures via flow-affected grain-size evolution. Notably, although we can produce the seismic shear wave trends of the LVZ regardless of the water content and flow configuration, this is not true of the low Q zone in the asthenosphere. For dry upper mantle flowing via Couette flow, the predicted seismic Q profile (Figure 5a) does not show a pronounced low Q zone in the asthenosphere. Instead, Q becomes approximately constant with depth and consistently < 50 despite an increase in grain-size with depth (6 mm – 30 mm, Figure 4b). In contrast, a wet upper mantle deformed via *PFn3* produces a zone of low seismic Q in the asthenosphere (Figure 5c). The magnitude and extent of this zone are affected by the plate velocity and pressure gradient combination because of the stress-dependent grain size evolution. Indeed, the grain-size structure produced by the *PFn3* configuration affects both the Q structure and the V_s profile. For instance, the Q and V_s peaks within the lower asthenosphere (200 – 250 km) are caused by the grain-size peak (Figure 4e) associated with weak shearing in this region. However, this is not evident for Couette-dominated dry asthenosphere because the grain size increase is much smaller (Figure 4b) than it is for *PFn3*-dominated wet asthenosphere (Figure 4e).

5.2 Comparison between theoretical seismic models and observations

In practice, reported Q models (Figure 5e) are globally-sourced profiles, which limits spatial resolution and may cancel out some localized features. The shear wave velocity observations presented here are averaged for oceanic plates of similar ages (i.e., mid-age plates, Figure 5f), and thus should be comparable with our curves for an assumed 60 Myr old oceanic plate (Figure 5b and 5d). However, because of averaging across plates with different speeds and pressure gradients, we are limited in our comparisons between predicted and observed Q and V_S, which assume single choices of these parameters. Instead, we compare overall trends between the theoretical and geophysical models, and later attempt to infer the dominant type of flow in the oceanic upper mantle from the seismic observations (Figure 7, Section 7).

Although the *PFn3* configuration produces a low Q zone that is comparable to the observations (Section 5.1), the predicted Q below the asthenosphere does not continue to increase for all cases (Figure 5c). Observations show Q>100 below the asthenosphere (Figure 5e), which requires grain-sizes larger than 10 cm (e.g., case i, Figure 4e). We may increase the grain size significantly (> 10 cm) by introducing high water content below the asthenosphere (Section 5.3) and low stresses that favor grain growth in this region. This requires a *PFn3* configuration that spans the entire upper mantle and mantle transition zone (i.e., case i, Figure 4d) and that is not confined to the upper mantle above 410 km (as for cases ii and iii).

5.3 Impact of partial melt and water distribution on seismic structures

The shallow upper mantle or asthenosphere has been proposed to be water-undersaturated and to contain unextractable melt (e.g., Selway and O'Donnell, 2019; Debayle et al, 2020), while the deeper upper mantle may contain no melt and a higher water content (e.g., Selway et al., 2019; Selway and O'Donnell, 2019). Here we test how such conditions would affect upper mantle flow and associated seismic observations. We consider a -1 kPa/km pressure gradient and a plate speed of 2 cm/yr (as in case i) and assume an increasing water content with depth in the upper mantle (Figure 6a.1). We compute the associated flow configuration (Figure S6a, Supplementray Information E.4), which is *PFn3* across the uppermost 670 km of the mantle, and the associated grain-size structure (Figure S6b). The predicted Q profile (pink line, Figure 6b) lies close to the observations and overlaps well with the Dalton et al. (2008) (D08) model

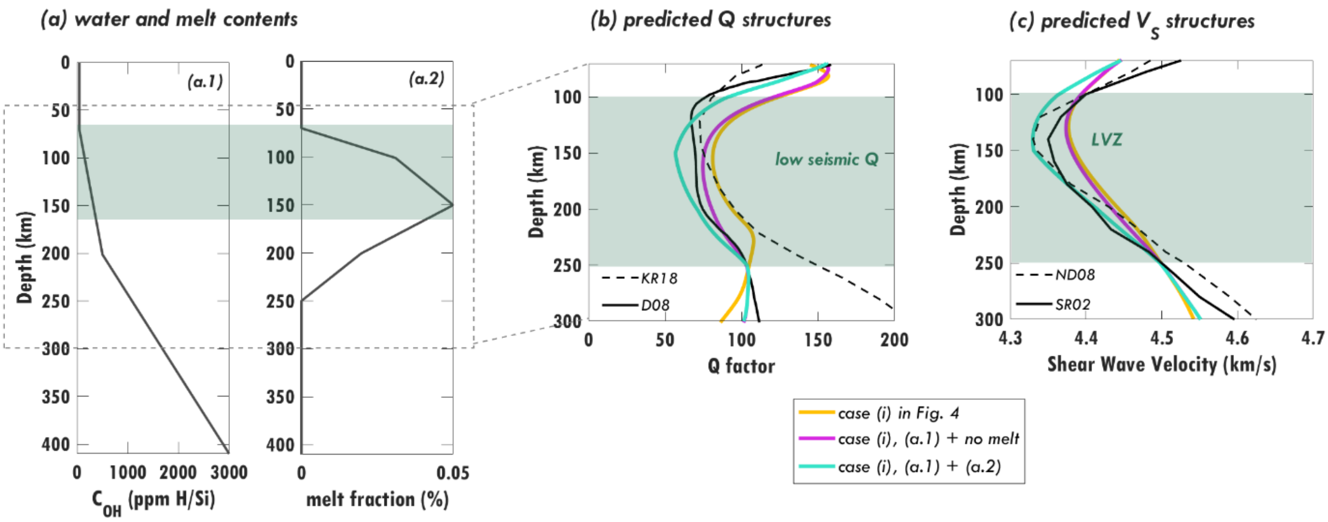

Figure 6. Impact of water content (a.1) and partial melt distribution (a.2) on predicted seismic structures (b-c). The melt fraction in the asthenosphere is calculated as x - 0.10% where x (in %) is estimated from Debayle et al. (2020) models for a plate moving with a speed of 2 cm/yr. The Jackson and Faul (2010) formulation for Q is used to predict the seismic structures for a melt-free upper mantle using the flow-induced grain sizes, and the Chantel et al. (2016) formulation is used in addition to Jackson and Faul (2010) when melt is present. The seismic observations in (b) and (c) are the same as in Figure 5e and f, respectively.

for mid-age plates in the lower asthenosphere. Below the asthenosphere, the predicted Q is larger than that of the constant-water (1000 ppm H/Si) assumption (yellow line, Figure 6b) and closer to observations. In contrast to the Q responses, the predicted V_S profiles for models with different water contents (yellow and pink lines, Figure 6c) mostly overlap and have larger minimum V_S in the LVZ than the observations.

We examine the effect of melt by introducing a melt distribution scenario (Figure 6a.2, $x-$ 0.10%) where x in % is estimated from Debayle et al. (2020) models for a plate moving with a speed of 2 cm/yr. We constrain the melt fraction to < 0.3%, which is the suggested melt fraction for the asthenosphere (e.g., Selway and O'Donnell, 2019; Debayle et al., 2020). This small amount of melt reduces the viscosity of the asthenosphere only slightly, by a factor greater than ~0.8, when using olivine flow laws (Equations 4 and 5.1 to 5.4), which has a negligible effect on upper mantle flow, grain-sizes, and rheology (Figure S6, Supplementary Information E.4). However, the additional melt does significantly affect seismic Q and V_S (Chantel et al., 2016). Adding melt into the asthenosphere of mostly wet upper mantle produces seismic V_S structures that follow the observations more closely than those of melt-free assumptions (light green line, Figure 6c). Overall, adding melt to the asthenosphere (which decreases both Q and V_S) and introducing high water content to the deep upper mantle (which increases grain size and Q) improves the fit to observations for our predicted seismic structures. Notably, a fast-moving plate (case iii, Figure 4d), which produces larger grain sizes in the asthenosphere (Figure 4e) than a slow plate (case ii), may require even more melt (Debayle et al., 2020) to reduce the seismic Q further.

6. Discussion

In this 1-D analytical study, we assume a composite rheology (dislocation and diffusion creep mechanisms) for olivine to represent the bulk rheology above 410 km since olivine is the most abundant and well-studied mineral. The inherent viscosity of other phases such as pyroxenes (e.g., Chen et al., 2006) and the effect of multiple phases on the overall rheology may additionally affect the predicted type of flow. We assume that the mantle transition zone has constant viscosity and flows under diffusion creep (*PFn1*-dominated). If the mantle transition zone is assumed to flow under dislocation creep with wet upper mantle above it (entirely *PFn3*-dominated above 670 km), this may increase the predicted Q below the asthenosphere where grain-sizes may increase due to low stresses induced by the *PFn3* configuration.

Empirically, seismic Q increases with increasing grain size (e.g., Jackson and Faul, 2010) but neither the magnitude nor the seismic period range of the minimum Q in the asthenosphere are well constrained by experiments. There may be other factors influencing attenuation that we do not account for in the estimation, such as oxygen fugacity that may decrease below the asthenosphere and can cause an increase in Q (e.g., Cline et al., 2018). In addition, we consider a single geological setting that is not perfectly comparable with the spherically averaged seismic Q models and velocity models, which may cancel out heterogeneities. Averaging our predicted seismic profiles across a range of imposed plate velocities and pressure gradients may improve the usefulness of our theoretical seismic models when compared to globally-averaged observations.

Since water distribution indirectly affects the prediction of seismic structures, accounting for inferred water contents from magnetotelluric (MT) surveys in the oceanic upper mantle (e.g., Selway et al., 2019) may improve our forward models. Although the small amount of melt fraction considered in this study, which is also detectable by MT surveys, has a negligible effect on the viscosity and flow configuration (Figure S6) when using olivine flow laws, it can potentially affect asthenospheric deformation if the melt is aligned (e.g., Wang et al. 2013; Hansen et al., 2021), and may have a significant impact on diffusion creep viscosity if the melt is well-connected (e.g., Holtzman, 2016).

The depth of base of the asthenosphere and the velocity boundary conditions there are not well constrained. This is why we extend our 1-D model to 670 km, which should reduce any boundary effects. However, we have found that the rheology contrast between the mantle transition zone and the overlying upper mantle significantly affects the distribution of flow between these layers (Figure S5) and is poorly constrained. Furthermore, the rheology of the mantle transition zone, and the mantle above it, may vary laterally because of lateral variations in hydration of the transition zone (e.g., Karlsen et al., 2019).

Since we consider 1-D mantle flow, we assume that pressure-driven flow and the surface plate move in the same direction. However, a possible transverse component of the horizontal pressure gradient relative to the plate motion (essentially a 2D problem) will affect the interaction between the two flows, particularly for non-Newtonian rheology (Natarov and Conrad, 2012), and thus also the predicted variations in grain size, seismic velocity, attenuation and anisotropy. Investigating such 2D variations is beyond the scope of this study.

7. Flow configurations for the upper mantle

Our models suggest four possible flow configurations (Figure 7a) above 670 km depth, depending on the drivers of the flow and the viscosity contrast between upper mantle and mantle transition zone:

[1] ***CF:*** Couette flow dominates across the uppermost 670 km if the upper mantle and mantle transition zone are both strongly viscous (e.g., if they are dry). This occurs if pressure gradients in the channel are not large enough to drive flow within the highly viscous channel.

[2] ***PFn1-MTZ:*** Poiseuille flow dominates in the MTZ with little deformation in the upper mantle if the mantle transition zone is significantly less viscous than the upper mantle. This is because higher viscosities in the upper mantle prevent deformation, which instead becomes

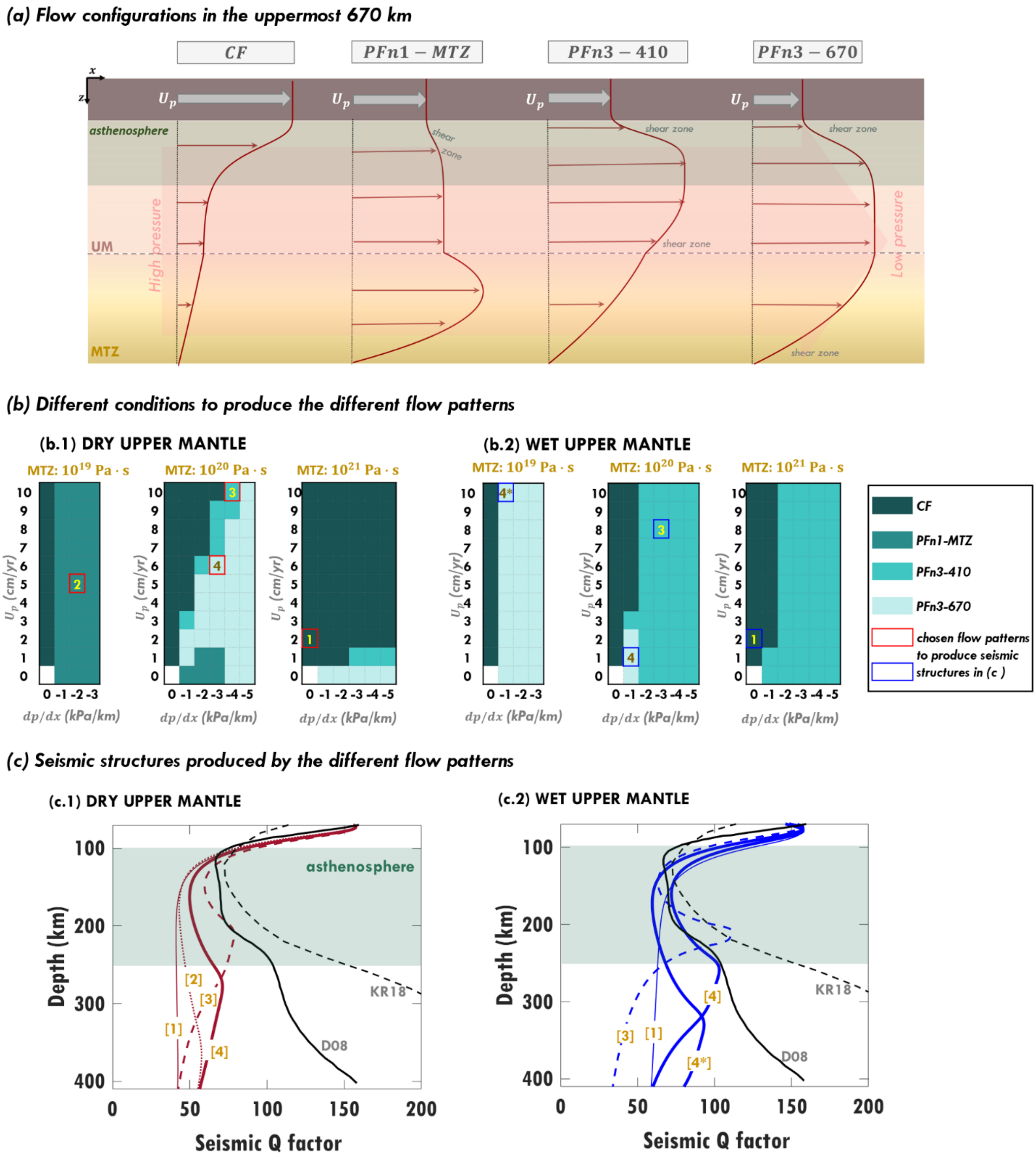

Figure 7. (a) A schematic diagram for different flow configurations that may dominate in the oceanic upper mantle and MTZ. (b) The dominant flow for different plate velocity (U_p) and horizontal pressure gradient (dp/dx) combinations for (b.1) dry (50 ppm H/Si) and (b.2) wet (1000 ppm H/Si) conditions, for different MTZ viscosities. (c) Predictions of seismic Q factor for different flow configurations for (c.1) dry and (c.2) wet conditions, where the type of flow configuration from (a) is indicated by a label [1]-[4] from (a) that also refers to the ($U_p, dp/dx$) combination used to drive the flow, as indicated in (b.1) and (b.2) above. Note that flow configuration [2] does not occur for wet conditions. Observations of seismic Q for comparison are the KR18 global Q model of Karaoglu and Romanowicz (2018) and the D08 model of Dalton et al. (2008) for mid-age oceans. Abbreviations: UM = upper mantle, MTZ = mantle transition zone, CF = Couette flow, and PF = Poiesuille flow (PFn1 for Newtonian PF and PFn3 for plug flow, see Figure 2a and 2b).

concentrated within the mantle transition zone that is assumed to have a Newtonian rheology (thus *PFn1*-dominated).

[3] *PFn3-410:* Plug flow occurs dominantly in the upper mantle if the mantle transition zone is more viscous than the upper mantle. Here deformation concentrates within the less viscous (typically wet) upper mantle, and the pressure gradient must be large enough that plug flow exceeds the plate-driven Couette flow.

[4] *PFn3-670:* Plug flow may dominate across the uppermost 670 km if both the upper mantle and mantle transition zone have sufficiently low viscosities (e.g., if they are wet) to allow existing pressure gradients to drive flow or if pressure gradients are large enough to drive plug flow in a viscous (dry) upper mantle.

Because of its impact on viscosity, water content helps to determine the dominant flow configuration (Figure 7b). A dry upper mantle (Figure 7b.1) may exhibit any of these four flow configurations, depending on the viscosity of mantle transition zone. A low-viscosity mantle transition zone (10^{19} Pa·s) exhibits dominantly *PFn1-MTZ*, an intermediate viscosity (10^{20} Pa·s) may produce any of the four configurations depending on flow drivers, and a highly viscous mantle transition zone (10^{21} Pa·s) is stiff enough to only produce the *CF* configuration. A wet upper mantle (Figure 7b.2) produces dominantly *PFn3* flow, either above 410 km if the mantle transition zone is stiff enough to prevent deformation or above 670 km otherwise.

Seismic Q and velocity profiles can potentially constrain mantle flow. However, most of the seismic structures reported are averaged globally or over a range of plate ages, which may cancel out some localized features such as the peak seismic velocity and the peak seismic Q within the asthenosphere, as predicted for *PFn3-410* (dashed lines labelled with [3], Figure 7c). This limits our ability to compare forward seismic velocity and attenuation models with most of the seismological observations, unless the observations are localized. Nonetheless, from our forward models, a dominant *PFn3-670* configuration in the oceanic mantle above 670 km (solid lines labelled with [4], Figure 7c) best explains the seismic Q minimum within the asthenosphere. For this flow configuration, magnitudes of Q for wet upper mantle (Figure 7c.2) are closer to the observations than those for dry upper mantle (Figure 7c.1) because the induced dry olivine grain-sizes are too small (< 3 cm, Figure S7c) to explain the Q observations, particularly beneath the asthenosphere.

8. Conclusions

As a summary, we propose the following to explain the observed seismic structures, particularly the observed low-Q zone:

(i) Poiseulle flow (*PF*), and particularly plug flow (*PFn3*), may dominate deformation within the oceanic upper mantle. Wet conditions facilitate this type of flow because they reduce upper mantle viscosity, allowing ambient mantle pressure gradients to drive plug flow that can overprint plate-driven shearing (Couette flow, *CF*).

(ii) Variations in grain size induced by plug flow (*PFn3*) are necessary to explain the zone of low Q (high seismic attenuation) in the asthenosphere. Here, low Q can be attributed to grain-size reduction due to extensive shearing within the low viscosity asthenosphere.

(iii) The increase of Q beneath the asthenosphere can be explained by large grain-sizes associated with minimal deformation within the ~250-410 km depth range. Such slow deformation is consistent with plug flow spanning the entire upper mantle and transition zone (the *PFn3-670* flow configuration, Figure 7a).

(iv) High water content may be required to promote large grain sizes (> 10 cm) in the mantle rocks beneath the asthenosphere.

(v) Melt in the asthenosphere is not necessary (e.g., Lin et al., 2016) to explain observed seismic anomalies there. Instead, grain-size variations associated with plug flow

(*PFn3*) can explain both the low-Q and low velocity zones (LVZ). Small amounts of melt can, however, amplify these trends, which can improve the fit to global seismic observations (e.g., Figure 6).

Pressure-driven flow travelling beneath the oceanic lithosphere is important because it promotes long-wavelength mantle convection (Semple and Lenardic, 2018), drives tectonic plate motions (Semple and Lenardic, 2020), transports geochemical heterogeneities (Yamamoto et al., 2007), and generates intraplate volcanism (Ballmer et al., 2013). Here we have shown that pressure-driven plug flow may additionally explain pervasive seismic observations such as the LVZ and the low-Q zone, by reducing asthenospheric grain-sizes. Because this grain-size reduction also weakens asthenospheric rocks, plug flow helps to maintain a low-viscosity asthenosphere, a key feature of Earth’s interior structure that regulates a variety of geodynamic process ranging from plate tectonics to postseismic and postglacial relaxation (e.g., Richards and Lenardic, 2018).

Acknowledgments

This work was supported partly by the Research Council of Norway's projects 223272 (Centre of Excellence) and 288449 (MAGPIE Project), and partly by the Australian Research Council grant FT150100541.

References

Austin, N.J., and Evans, B. (2007). Paleowattmeters: A scaling relation for dynamically recrystallized grain size. *Geology, 35*, 343-346. doi:10.1130/G23244A.1

Ballmer, M. D., Conrad, C. P., Smith, E. I. and Harmon, N. (2013). Non-hotspot volcano chains produced by migration of shear-driven upwelling toward the East Pacific Rise. *Geology, 41*, 479-482, doi:10.1130/g33804.1.

Becker, T. (2006). On the effect of temperature and strain-rate dependent viscosity on global mantle flow, net rotation, and plate-driving forces. *Geophys. J. Int., 167*, 943-957. doi: 10.1111/j.1365-246X.2006.03172.x

Behn, M., Hirth, G. and Elsenbeck II, J. R. (2009). Implications of grain size evolution on the seismic structure of the oceanic upper mantle. *Earth and Planetary Science Letters, 282*, 178-189. doi: 10.1016/j.epsl.2009.03.014

Chantel, J., Manthilake, G., Andrault, D., Novella, D., Yu, T., and Wang, Y. (2016). Experimental evidence supports mantle partial melting in the asthenosphere. *Science Advances, 2*, e1600246. doi:10.1126/sciadv.1600246

Cline II, C., Faul, U., David, E., Berry, A., and Jackson, I. (2018). Redox-influenced seismic properties of upper-mantle olivine. *Nature, 555*, 355-358. doi:10.1038/nature25764

Dalton, C., Ekström, G., and Dziewonski, A. (2008). The global attenuation structure of the upper mantle. J. *Geophys. Res. 113*, B09303. doi:10.1029/2007JB005429

Dalton, C., Ekström, G., and Dziewonski, A. (2009). Global seismological shear velocity and attenuation: A comparison with experimental observations. Earth and Planetary Science Letters 284, 65-75. doi:10.1016/j.epsl.2009.04.009

Debayle, E., Bodin, T., Durand, S. and Ricard, Y. (2020). Seismic evidence for partial melt below tectonic plates. *Nature, 586*, 555-559. doi:10.1038/s41586-020-2809-4

Faul, U. and Jackson, I. (2005). The seismological signature of temperature and grain size variations in the upper mantle. *Earth and Planetary Science Letters, 234*, 119-134. doi:10.1016/j.epsl.2005.02.008

Forte, A., and Mitrovica, J. (1996). New inferences of mantle viscosity from joint inversion of long-wavelength mantle convection and post-glacial rebound data. *Geophys. Res. Lett. 23*, 1147-1150. doi:10.1029/96GL00964

Gutenberg (1959), *Physics of the Earth's Interior*, Springer, New York.

Hall, C. and Parmentier, E.M. (2003). Influence of grain size evolution on convective instability. *Geochem. Geophys. Geosyst., 4*, 1029. doi:10.1029/2002GC000308

Hansen, L., Faccenda, M., and Warren, J. (2021). A review of mechanisms generating seismic anisotropy in the upper mantle. *Physics of the Earth and Planetary Interiors 313*, 106662. doi: 10.1016/j.pepi.2021.106662

Hirth, G., and Kohlstedt, D. (2003). Rheology of the Upper Mantle and the Mantle Wedge: A View from the Experimentalists. *Inside the Subduction Factory, Geophysical Monograph, 138*, 83-105.

Höink, T., and Lenardic, A. (2010). Long wavelength convection, Poiseuille–Couette flow in the low-viscosity asthenosphere and the strength of plate margins. *Geophys. J. Int. 180*, 23–33. doi: 10.1111/j.1365-246X.2009.04404.x.

Holtzman, B. (2016). Questions on the existence, persistence, and mechanical effects of a very small melt fraction in the asthenosphere. Geochem. Geophys. Geosys., 17, 470-484. https:doi:10.1002/2015GC006102.

Jackson, I., and Faul, U. (2010). Grainsize-sensitive viscoelastic relaxation in olivine: Towards a robust laboratory-based model for seismological application. *Physics of the Earth and Planetary Interiors, 183*, 151-163. doi:10.1016/j.pepi.2010.09.005

Jung, H. and Karato, S. (2001). Water-induced fabric transitions in olivine, *Science, 293*, 1460-1463. doi:10.1126/science.1062235

Karaoglu, H. and Romanowicz, B. (2018). Inferring global upper-mantle shear attenuation structure by waveform tomography using spectral element method. *Geophys. J. Int.*, *213*, 1536-1558. doi: 10.1093/gji/ggy030

Karato, S.-i. (1993). Importance of anelasticity in the interpretation of seismic tomography. *Geophys. Res. Lett.*, *20*, 1623-1626. https://doi.org/10.1029/93GL01767

Karato, S.-i. (2012). On the origin of the asthenosphere, *Earth and Planetary Science Letters 321-322*, 95-103. doi:10.1016/j.epsl.2012.01.001

Karato, S.-i., and Jung. H. (1998), Water, partial melting and origin of the seismic low velocity and high attenuation zone in the upper mantle, *Earth and Planetary Science Letters 157*, 193-207.

Karlsen, K., Conrad, C. and Magni, V. (2019). Deep water cycling and sea level change since the breakup of Pangea. *Geochemistry, Geophysics, Geosystems*, *20*, 2919–2935. doi: 10.1029/2019GC008232

Kaufmann, G. and Lambeck, K. (2000). Mantle dynamics, postglacial rebound and the radial viscosity profile. *Physics of the Earth and Planetary Interiors 121*, 301-324. doi:10.1016/s0031-9201(00)00174-6

Lin, P.Y.P., Gaherty, J.B., Jin, G., Collins, J.A., Lizarralde, D., Evans, R.L., and Hirth, G. (2016). High-resolution seismic constraints on flow dynamics in the oceanic asthenosphere. *Nature 535*, 538–541. doi: 10.1038/nature18012

Mei, S., and Kohlstedt, D. L. (2000). Influence of water on plastic deformation of olivine aggregates: 1. Diffusion creep regime. *Journal of Geophysical Research, 105*, 21457-21469. doi: 10.1029/2000jb900179

Natarov, S. and Conrad, C.P. (2012). The role of Poiseuille flow in creating depth-variation of asthenospheric shear. *Geophys. J. Int.* 190, 1297-1310. doi: 10.1111/j.1365-246X.2012.05562.x

Nettles, M. and Dziewonski, A. (2008). Radially anisotropic shear velocity structure of the upper mantle globally and beneath North America. *Journal of Geophysical Research, 113*, B02303. doi:10.1029/2006JB004819

Richards, M., Yang, W.-S., Baumgardner, J. and Bunge, H.-P. (2001). Role of a low-viscosity zone in stabilizing plate tectonics: Implications for comparative terrestrial planetology. *Geochem. Geophys. Geosyst., 2*, 2000GC000115. doi:10.1029/2000GC000115

Richards, M. A., and A. Lenardic (2018). The Cathles Parameter (Ct): A Geodynamic Definition of the Asthenosphere and Implications for the Nature of Plate Tectonics. *Geochemistry, Geophysics, Geosystems*, *19(12)*, 4858-4875, doi:10.1029/2018GC007664.

Ritterbex, S., Carrez, P. and Cordier, P. (2020). Deformation across the mantle transition zone: A theoretical mineral physics view. *Earth and Planetary Science Letters, 547*, 116438. doi: 10.1016/j.epsl.2020.116438

Selway, K., and O'Donnell, J. (2019). A small unextractable melt fraction as the cause for the low velocity zone. *Earth and Planetary Science Letters, 517*, 117-124. doi:10.1016/j.epsl.2019.04.012

Selway, J., O'Donnell, J.P., and Özaydin, S. (2019). Upper Mantle Melt Distribution From Petrologically Constrained Magnetotellurics. Geochem. Geophys. Geosys. 20, 3328-3346. doi: 10.1029/2019GC008227

Semple, A. and Lenardic, A. (2018). Plug flow in the Earth's asthenosphere. *Earth and Planetary Science Letters, 496*, 29-36. doi: 10.1016/j.epsl.2018.05.030

Semple, A., and Lenardic, A. (2020). The Robustness of Pressure-Driven Asthenospheric Flow in Mantle Convection Models With Plate-Like Behavior, *Geophysical Research Letters, 47(17)*, e2020GL089556, doi:10.1029/2020gl089556.

Shapiro, N.M. and Ritzwoller, M.H. (2002). Monte-Carlo inversion for a global shear-velocity model of the crust and upper mantle. *Geophys. J. Int. 151*, 88-105. doi:10.1046/j.1365-246X.2002.01742.x

Steinberger, B. and Calderwood, A. (2006). Models of large-scale viscous flow in the Earth's mantle with constraints from mineral physics and surface observations. *Geophys. J. Int. 167*, 1461-1481. doi: 10.1111/j.1365-246X.2006.03131.x

Tommasi, A., Tikoff, B. and Vauchez, A. (1999). Upper mantle tectonics: three-dimensional deformation, olivine crystallographic fabrics and seismic properties. *Earth and Planetary Science Letters*, *168*, 173-186. doi:10.1016/S0012-821X(99)00046-1

Turcotte, D., and Schubert, G. (2014). *Geodynamics* (3rd ed.). New York: Cambridge University Press.

Wang, N., Montagner, J.P., Fichtner, A., and Capdeville, Y. (2013). Intrinsic versus extrinsic seismic anisotropy: The radial anisotropy in reference Earth models. *Geophys. Res. Lett., 40*, 4284-4288. doi: 10.1002/grl.50873

Warren, J. and Hirth, G. (2006). Grain size sensitive deformation mechanisms in naturally deformed peridotites. *Earth and Planetary Science Letters, 248*, 438-450. doi:10.1016/j.epsl.2006.06.006

Yamamoto, M., Morgan, J. P., Morgan, W. J., Foulger, G. R. and Jurdy, D. M. (2007). Global plume-fed asthenosphere flow—I: Motivation and model development, in Plates, Plumes and Planetary Processes, edited, p. 0, Geological Society of America, doi:10.1130/2007.2430(09).

Supplementary Information

A. Predicted seismic structures for non-deforming oceanic upper mantle

For an oceanic upper mantle that is not deforming, we assume that the grain size is constant. We consider different grain sizes (1 mm – 10 cm) and calculate their respective seismic structures (blue lines, Figure S1). As expected, Q values (Figure S1a) within the upper mantle are larger for larger grain size, resulting in faster seismic velocities (Figure S1b) than for smaller grain size. Notably, a LVZ can be produced (Figure S1b) but not the low Q zone (Figure S1a).

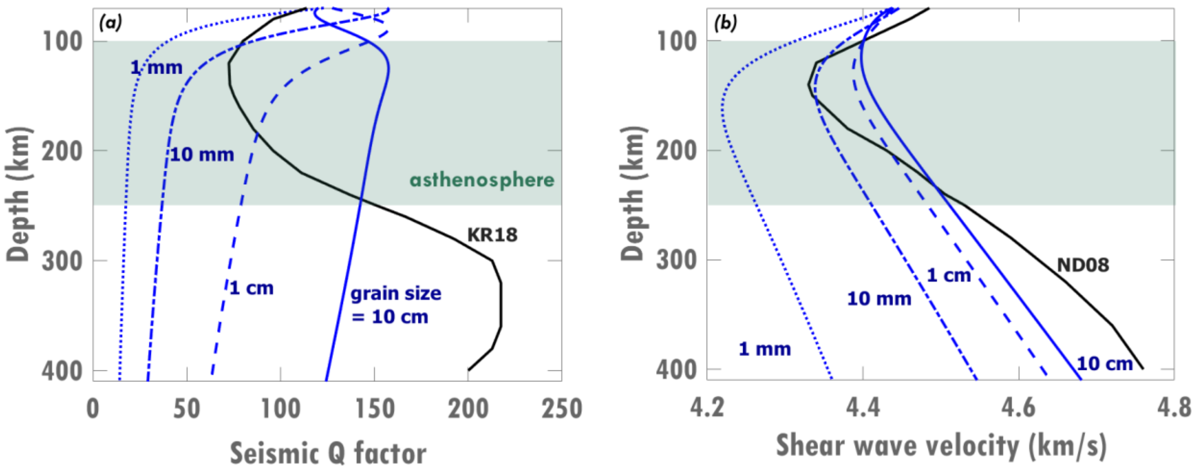

Figure S1. Seismic structures for oceanic upper mantle that is not deforming. (a) The seismic Q structures are calculated using Faul and Jackson's (2010) formulation for 100 s period, where Q is sensitive to a chosen grain size (values given), which is assumed constant in the absence of deformation. The global KR18 model is from Karaoglu & Romanowicz (2018). (b) The associated forward shear wave velocities are estimated using Karato's (1993) formulation, again for constant chosen grain size. The global ND08 model is from Nettles & Dziewonski (2008).

B. Analytical solution for 1-D rheology-dependent mantle flow in N layers

To implement composite rheology in the upper mantle, we must combine both Newtonian Poiseuille flow (*PFn1*) and plug flow (*PFn3*) models. For an assigned Newtonian rheology for the mantle transition zone, we only use the *PFn1* model. We apply Equations (3) and (6.2) and the boundary conditions shown in Figure S2 and summarized below:

$$v_{x,1}(z_0) = U_p \tag{S1}$$

$$v_{x,N}(z_N) = 0 \tag{S2}$$

$$\text{at } z_i\text{:} \quad \tau_i(bottom\ boundary\ of\ ith\ layer) = \tau_{i+1}(top\ boundary\ of\ ith+1\ layer) \tag{S3}$$

$$\text{at } z_i\text{:} \quad v_{x,i}(bottom\ boundary\ of\ ith\ layer) = v_{x,i+1}(top\ boundary\ of\ ith+1\ layer) \tag{S4}$$

This yields a set of equations:

$$\frac{\partial p}{\partial x} z_i + C_i = \frac{\partial p}{\partial x} z_i + C_{i+1} \rightarrow C_i = C_{i+1} \tag{S5}$$

$$A_{PFn1,i}\left[\frac{1}{2}\frac{\partial p}{\partial x} {z_i}^2 + C_i z_i\right] + A_{PFn3,i}\left[\begin{array}{c}\frac{1}{4}\left(\frac{\partial p}{\partial x}\right)^3 {z_i}^4 + C_i\left(\frac{\partial p}{\partial x}\right)^2 {z_i}^3 \\ +\frac{3}{2}{C_i}^2\frac{\partial p}{\partial x}{z_i}^2 + {C_i}^3 z_i\end{array}\right] + k_i =$$

$$A_{PFn1,i+1}\left[\frac{1}{2}\frac{\partial p}{\partial x} {z_i}^2 + C_{i+1} z_i\right] + A_{PFn3,i+1}\left[\begin{array}{c}\frac{1}{4}\left(\frac{\partial p}{\partial x}\right)^3 {z_i}^4 + C_{i+1}\left(\frac{\partial p}{\partial x}\right)^2 {z_i}^3 \\ +\frac{3}{2}{C_{i+1}}^2\frac{\partial p}{\partial x}{z_i}^2 + {C_{i+1}}^3 z_i\end{array}\right] + k_{i+1} \tag{S6}$$

We linearize the equations by grouping the terms in Equations (S5) and (S6) such that the terms with first degree C's and k's (constants of integration) are on the left side of the equation and the remaining terms are on the right side. Then, we can express the boundary conditions for the layered system as *M***R**=**A** where vector **R** contains the constants of integration (C's and k's) and vector **A** has the higher degree C's:

$$\begin{pmatrix} a_{PFn1,1}+a_{PFn3,1} & 1 & 0 & 0 & 0 & 0 & \dots & 0 & 0 & 0 & 0 \\ a_{PFn1,1}+a_{PFn3,1} & 1 & -(a_{PFn1,2}+a_{PFn3,2}) & -1 & 0 & 0 & \dots & 0 & 0 & 0 & 0 \\ 1 & 0 & -1 & 0 & 0 & 0 & \dots & 0 & 0 & 0 & 0 \\ 0 & 0 & a_{PFn1,2}+a_{PFn3,2} & 1 & -(a_{PFn1,3}+a_{PFn3,3}) & -1 & \dots & 0 & 0 & 0 & 0 \\ 0 & 0 & 1 & 0 & -1 & 0 & \dots & 0 & 0 & 0 & 0 \\ \vdots & \vdots & \vdots & \vdots & \vdots & \vdots & \ddots & \vdots & \dots & \vdots & \vdots \\ 0 & 0 & 0 & 0 & 0 & 0 & \dots & a_{PFn1,N-1}+a_{PFn3,N-1} & 1 & -(a_{PFn1,N}+a_{PFn3,N}) & -1 \\ 0 & 0 & 0 & 0 & 0 & 0 & \dots & 1 & 0 & -1 & 0 \\ 0 & 0 & 0 & 0 & 0 & 0 & \dots & 0 & 0 & a_{PFn1,N}+a_{PFn3,N} & 1 \end{pmatrix} \begin{pmatrix} C_1 \\ k_1 \\ C_2 \\ k_2 \\ C_3 \\ k_3 \\ \vdots \\ C_{N-1} \\ k_{N-1} \\ C_N \\ k_N \end{pmatrix}$$

$$= \begin{pmatrix} -(b_{PFn1,1}+b_{PFn3,1})+U_p \\ -(b_{PFn1,1}+b_{PFn3,1})+(b_{PFn1,2}+b_{PFn3,2}) \\ 0 \\ -(b_{Pn1F,2}+b_{PFn3,2})+(b_{PFn1,3}+b_{PFn3,3}) \\ 0 \\ \vdots \\ -(b_{PFn1,N-1}+b_{PFn3,N-1})+(b_{PFn1,N}+b_{PFn3,N}) \\ 0 \\ -(b_{PFn1,N}+b_{PFn3,N}) \end{pmatrix} \tag{S7}$$

where,

$$a_{PFn1,i} = A_{PFn1,i}\, z_i \tag{S8}$$

$$a_{PFn3,i} = A_{PFn3,i} \left(\frac{\partial p}{\partial x}\right)^2 {z_i}^3 \tag{S9}$$

$$b_{PFn1,i} = \frac{1}{2} A_{PFn1,i} \frac{\partial p}{\partial x} {z_i}^2 \tag{S10}$$

$$b_{PFn3,i} = A_{PFn3,i} \begin{bmatrix} \frac{1}{4}\left(\frac{\partial p}{\partial x}\right)^3 {z_i}^4 + \\ + \frac{3}{2} {C_i}^2 \frac{\partial p}{\partial x} {z_i}^2 + {C_i}^3 z_i \end{bmatrix} \tag{S11}$$

The terms $A_{PFn1,i}$ and $A_{PFn3,i}$ for the upper mantle are defined in Equations (5.3) and (5.4), respectively. For the mantle transition zone (MTZ), $A_{PFn1,i} = 2/\eta_{MTZ}$ and $A_{PFn3,i} = 0$. The higher degree C_i terms in Equation (S11) or in vector **A** are considered constant and we initially guess them to be the same for every layer i (as in Equation S5) to determine the C_i and k_i in vector **R** by inversion (**R**=M^{-1}**A**). Then, the C_i in vector

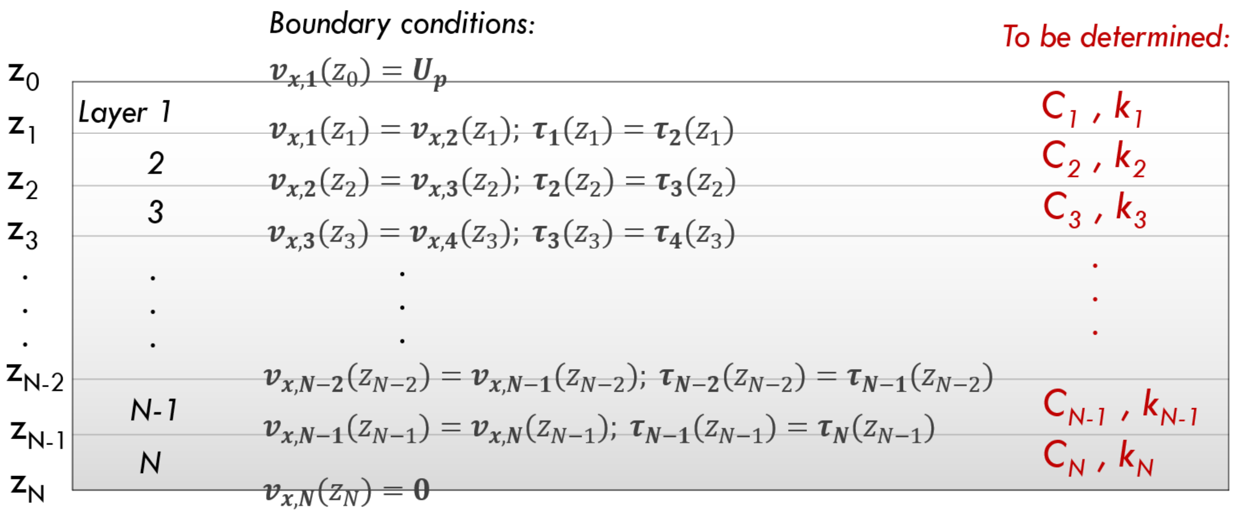

Figure S2. The boundary conditions for 1D model with N layers in terms of stress τ_i and flow horizontal velocity $v_{x,i}$ where i is the layer number**.** The C_i and k_i integration constants in Equation (3) for stress and Equation (6.2) for flow velocity are determined, which allows us to solve stresses and flow velocities within the model.

A is updated in every iteration with the calculated C_i in vector **R** until their absolute difference is $\leq 10^{-6}$. Then, stresses (Equation 3) and velocities (Equation 6.2) with depth can be calculated using the derived C_i and k_i from vector **R**.

C. Iteration scheme to compute steady state grain size and stress evolution

The $A_{PFn1,i}$ and $A_{PFn3,i}$ parameters used in calculating stress τ and horizontal velocity v_x (Section A) are dependent on grain-size, which evolves with time (Equation 7). Both τ and v_x reach a steady state, which is determined by employing the scheme below:

$$\boldsymbol{t_0}: \quad \textit{assume constant } d_0 \rightarrow \textit{calculate } v_{x,t_0} \textit{ and } \tau_{t_0}$$

$$\boldsymbol{t_1 = t_0 + \Delta t}: \quad \textit{calculate } \Delta d_1 \textit{ and } d_1 \rightarrow \textit{calculate } v_{x,t_1} \textit{ and } \tau_{t_1}$$

$$\boldsymbol{t_2 = t_1 + \Delta t}: \quad \textit{calculate } \Delta d_2 \textit{ and } d_2 \rightarrow \textit{calculate } v_{x,t_2} \textit{ and } \tau_{t_2}$$

$$\vdots$$

$$\boldsymbol{t_k = t_{k-1} + \Delta t}: \quad \textit{calculate } \Delta d_k \textit{ and } d_k \rightarrow \textit{calculate } v_{x,t_k} \textit{ and } \tau_{t_k}$$

where

$$t_k = k\Delta t = grain\ size\ evolution\ time$$

$$\Delta t = change\ in\ time\ or\ time\ interval$$

$$d_k = new\ grain\ size\ structure\ after\ t_k\ (Equation\ (S12))$$

$$\Delta d_k = change\ in\ grain\ size\ after\ t_k\ (Equation\ \ (S13))$$

$$v_{x,t_k} = horizontal\ velocity\ profile\ of\ the\ flow\ at\ t_k$$

$$\tau_{t_k} = stress\ profile\ induced\ by\ the\ flow\ at\ t_k$$

After time t_k (which is $t_{k-1} + \Delta t$), we determine the new grain size structure d_k:

$$d_k = d_{k-1} + \Delta d_k \tag{S12}$$

where Δd_k is estimated by multiplying the grain-size change rate $\dot{d}_{k-1}$ at t_{k-1} by Δt:

$$\Delta d_k = \ \Delta t\left[\dot{d}_{k-1}\right] = \Delta t\left[\dot{d}_{gg,k-1} - \dot{d}_{dr,k-1}\right] \tag{S13}$$

Here $\dot{d}_{k-1}$ is estimated using Equation (7) where $\dot{d}_{gg,k-1}$ is the grain growth term and $\dot{d}_{dr,k-1}$ is the dynamic recrystallization term (the first and second terms on the right hand side of Equation (7), respectively). The constants used in the calculation of $\dot{d}$ (as described by Equations (7) and (S13)) are summarized in Table S1. Using the new d_k, we recalculate the horizontal velocity, shear stress, and viscosity structures. We iterate this process until a steady state grain size is reached at steady-state time t_{ss} (typically << 1 Myr, criterion is discussed in Section D).

Table S1. Grain size evolution parameters are taken from Behn et al. (2009) since they are calibrated to laboratory data, and the flow law parameters are from Hirth and Kohlstedt (2003).

Symbol	Description	Value		Units
$\dot{d}_{gg}$	Grain growth rate			m/s
$\dot{d}_{dr}$	Dynamic recrystallization rate			m/s
τ	Shear stress			Pa
σ	Differential stress (2τ)			Pa
p_g	Grain growth exponent	3		
G_o(dry)	Grain growth constant for 50 ppm H/Si	1.5×10^{-5}		$m^{p_g} s^{-1}$
G_o(wet)	Grain growth constant for 1000 ppm H/Si	4.5×10^{-4}		$m^{p_g} s^{-1}$
E_g	Activation energy for grain growth	350		kJ/mol
V_g	Activation volume for grain growth	4×10^{-6}		m^3/mol
λ	Reciprocal of strain required for new grain size	10		
χ	Fraction of work done by dislocation to ground boundary area	0.1		
c	Geometrical constant	3		
γ	Average specific grain boundary energy	1		J/m^2
$\dot{\varepsilon}_{disl}$	Dislocation creep strain rate	*For olivine*		s^{-1}
		DRY	WET	
A_{disl}	Dislocation creep prefactor	1.1×10^5	30	$MPa^{-3.5} s^{-1}$
n_{disl}	Dislocation creep stress exponent	3.5	3.5	
p_{disl}	Dislocation creep grain size exponent	0	0	
r_{disl}	Dislocation creep water exponent	0	1.2	
α_{disl}	Constant for melt factor	45	45	

E_{disl}	Dislocation creep activation energy	530	480	kJ/mol
V_{disl}	Dislocation creep activation volume	15×10^{-6}	11×10^{-6}	m^3/mol
$\dot{\varepsilon}_{diff}$	Diffusion creep strain rate	*For olivine*		s^{-1}
		DRY	WET	
A_{diff}	Diffusion creep prefactor	1.5×10^9	1×10^6	$MPa^{-3.5}s^{-1}$
n_{diff}	Diffusion creep stress exponent	1	1	
p_{diff}	Diffusion creep grain size exponent	3	3	
r_{diff}	Diffusion creep water exponent	0	1	
α_{diff}	Constant for melt factor	30	30	
E_{diff}	Diffusion creep activation energy	375	335	kJ/mol
V_{diff}	Diffusion creep activation volume	6×10^{-6}	4×10^{-6}	m^3/mol

D. Convergence criterion for grain size evolution

To determine the steady-state time t_{ss}, we employ a convergence criterion of:

$$\frac{\Delta d_{norm}}{d_{norm}} \leq \vartheta \qquad \text{(S14)}$$

where ϑ is the limit for convergence, Δd_{norm} is the depth-averaged norm of grain size change, and d_{norm} is the depth-averaged norm of grain size. As a convergence criterion, we use Equation (S15) for a chosen timestep Δt. At time t_k, the parameters in Equation (S14) are calculated as:

$$\vartheta = 5 \times 10^{-4} \left(\frac{\Delta t}{1000\ yr}\right) \qquad \text{(S15)}$$

$$\Delta d_{norm} = \frac{\sqrt{\sum_{i=1}^{N+1} (d_k - d_{k-1})^2 \Delta z}}{\sum_{i=1}^{N+1} \Delta z} \qquad \text{(S16)}$$

$$d_{norm} = \frac{\sqrt{\sum_{i=1}^{N+1} {d_k}^2 \Delta z}}{\sum_{i=1}^{N+1} \Delta z} \tag{S17}$$

When the criterion in Equation (S14) is met, $t_k \sim t_{ss}$.

E. Additional analyses at steady-state

E.1 Effect of initial grain-size

We compare two steady-state calculations that are the same except for different initial olivine grain-sizes (1 mm or 10 mm), which produces flow via Couette flow (*CF*) above a 10^{21} Pa·s mantle transition zone as shown in Figure S3a. Such a flow configuration

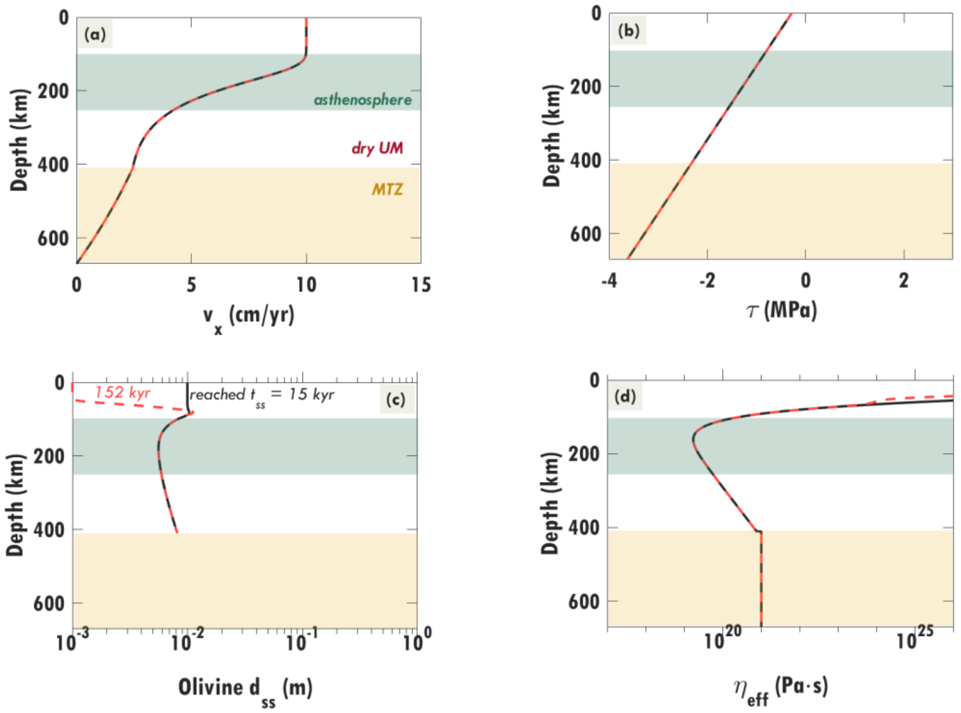

Figure S3. Effect of initial grain size (1 mm and 10 mm for the red dashed and black lines, respectively) on the steady-state (a) upper mantle flow, (b) induced shear stresses, (c) grain-size structure, and (d) effective viscosity. We assume dry conditions, and that the 60 Myr old oceanic upper mantle and mantle transition zone are deformed by plate motion of 10 cm/yr and a pressure gradient of -5kPa/km. Until the flow reaches steady state, grain size changes according to the grain size evolution AE07 model (Austin and Evans, 2007). Flow additionally alters the grain-size structure, which in turn changes the flow and rheology with time. The flow eventually reaches steady state after a time t_{ss}=152 kyr for an initial grain size of 1 mm and t_{ss}=15 kyr for an initial grain size of 10 mm (see Supplementary Information D). The timesteps Δt used for 1-mm and 10-mm flow models are 10 yr and 100 yr, respectively.

dominates because of large viscosities in the upper mantle and mantle transition zone (Figure S3d). Initially smaller (1 mm) and larger grain-sizes (10 mm) evolve to the same steady-state grain-size structure (except for the stiff undeforming lithosphere, Figure S3c) and the same steady-state upper mantle flow (Figure S3a) with the same stress profile (Figure S3b). Clearly, the choice of initial grain-size does not affect the system's eventual steady-state but it does affect the time it takes the grain size to reach steady state. A larger initial grain size (i.e., 10 mm) stabilizes faster (15 kyr) compared to a smaller grain size (1 mm, 152 kyr), because large grain-sizes subdivide rapidly (Equation 7).

E.2 Effect of grain-size evolution model

Hall & Parmentier (2003) provide another grain-size evolution model (HP03 model):

$$\textit{HP03 model}: \quad \dot{d} = {p_g}^{-1} d^{1-p_g} G_o \exp\left(-\frac{E_g + PV_g}{RT}\right) - \lambda \dot{\varepsilon}_{disl} d \qquad \text{(S18)}$$

The grain-size structure stabilizes faster when using AE07 model ($t_{ss} = 478\ kyr$) compared to using the HP03 model (598 kyr) because of AE07's strong dependence on grain-size (Figure S4c). Although the HP03 model (red dashed line, Figure S4c) predicts larger grain sizes than does the AE07 model (black line), their flow configurations (Poiseuille flow or PF, Figure S4a), stress profiles (Figure S4b), and viscosities (Figure S4d) are nearly the same.

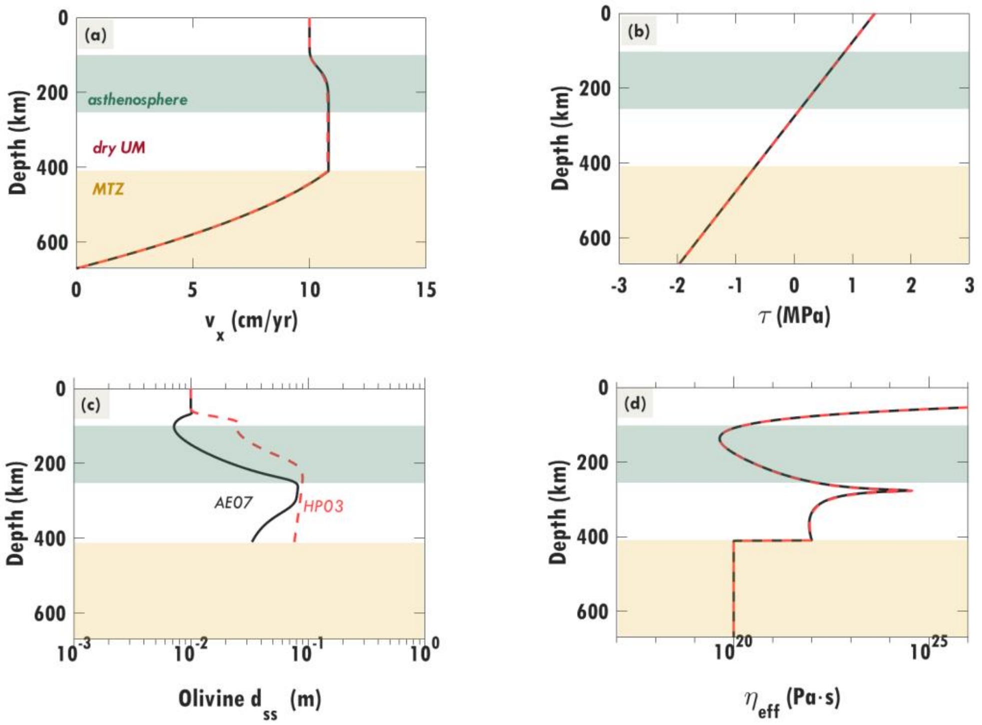

Figure S4. Effect of grain size evolution model (HP03 (Hall & Parmentier, 2003) for the red dashed line and AE07 (Austin and Evans, 2007) for the black line) on the steady-state (a) upper mantle flow, (b) induced shear stresses, (c) grain-size structure (initially 10 mm grain size), and (d) viscosity. The flow conditions considered are the same as in Figure S3. The timesteps Δt used for HP03 and AE07 grain-size evolution models are 1000 yr and 100 yr, respectively.

E.3 Effect of contrasting rheologies between upper mantle and MTZ

In Section 4, the comparable effective viscosities of upper mantle and mantle transition zone result in a *CF*-dominated dry upper mantle and a *PF*-dominated wet upper mantle. However, with contrasting rheologies, the dry upper mantle can accommodate a *PF* configuration (case ii, Figure S5a) and a *CF* configuration in wet upper mantle (case i, Figure S5d). The less viscous mantle transition zone below dry upper mantle (Figure S5c) allows a pressure-driven flow within the upper mantle (case ii, Figure S5a). In contrast, the more viscous mantle transition zone below the wet upper mantle (Figure S5f) can shut down pressure-driven flow unless the pressure gradient is large enough (cases ii and iii, Figure S5d) to drive *PF* that exceeds the plate-driven flow.

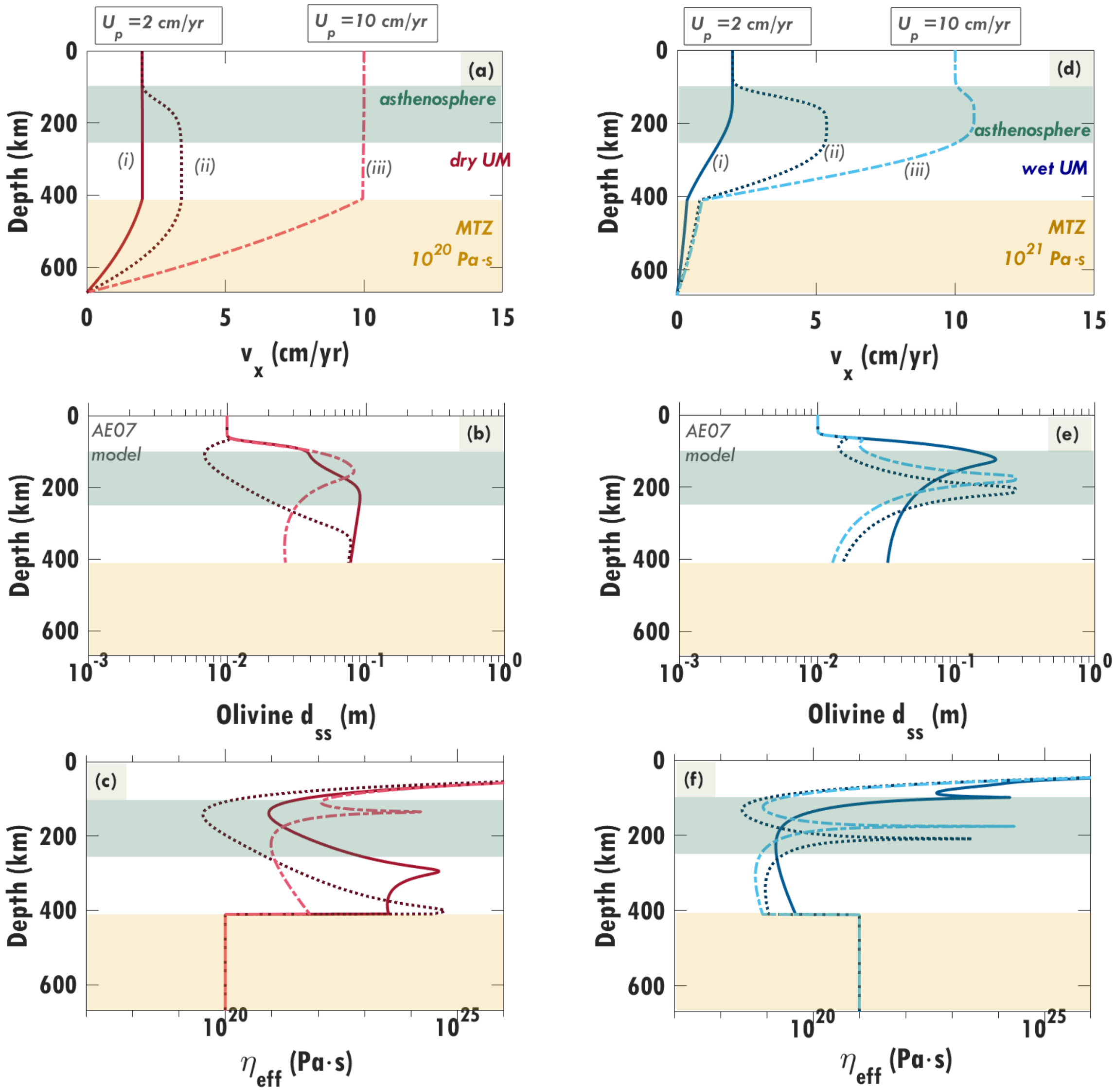

Figure S5. Effect of contrasting rheologies between upper mantle (UM) and MTZ on the steady state (a, d) flow, (b, e) grain size structure, and (c, f) viscosity for (a-c) dry and (d-f) wet (d-f) conditions. Different combinations of plate velocity and horizontal pressure gradient (labeled as i, ii and iii) are considered, and are the same as in Figure 4. For dry upper mantle, the assigned mantle transition zone (MTZ) viscosity is 10^{20} Pa·s, and 10^{21} Pa·s MTZ for wet upper mantle. The less viscous MTZ viscosity allows for a PF configuration to dominate in the more viscous upper mantle. Otherwise, CF may dominate unless the pressure gradient is large enough to drive PF that exceeds plate velocity. The initial grain-size for each calculation is 10 mm. A timestep Δt of 1000 yr is used for case (i), and 100 yr for cases (ii) and (iii).

E.4 Effect of water and small melt fraction on upper mantle flow and rheology

Varying the water distribution (blue line in Figure S6 vs. case (i) wet upper mantle in Figure 4) clearly alters the rheology and grain-size structures, and thus also the flow pattern. In contrast, adding a small amount of melt (< 0.1%, Figure 6a.2) in the

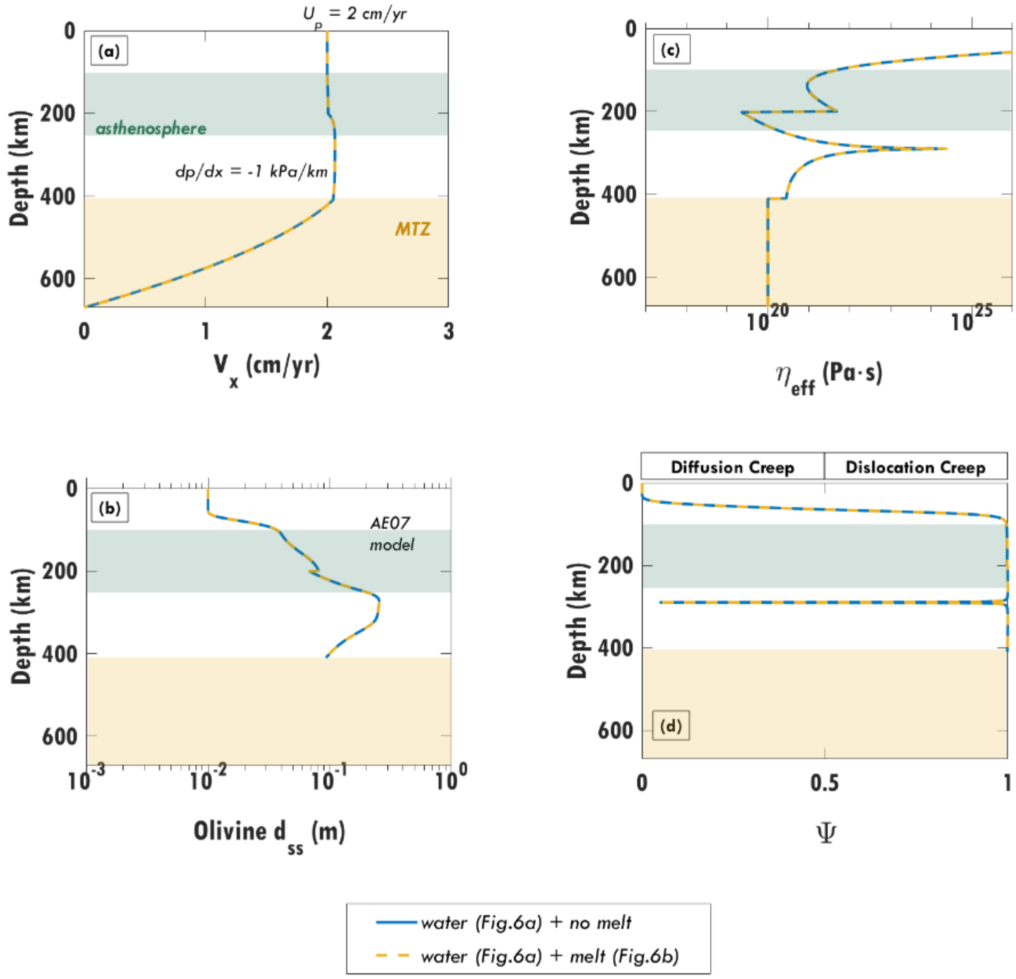

Figure S6. Effect of excluding melt (blue line) vs. including melt (dashed orange line) on steady-state upper mantle (a) flow, (b) olivine grain sizes, (c) viscosity, and (d) dominant deformation mechanism. A 60 Myr old oceanic upper mantle is considered with 2 cm/yr plate velocity and a -1 kPa/km pressure gradient. The grain-size evolution model used is AE07 (Austin and Evans, 2007) with a timestep Δt of 1000 yr.

asthenosphere reduces the viscosity by at least a factor of ~0.8, which yields negligible changes to the flow pattern and grain-size structure (compare blue and dashed orange lines, Figure S6).

E.5 Different flow configurations in dry and wet upper mantle

The flow configurations and rheological structures for the different plate velocity and pressure gradient combinations, and MTZ viscosities, shown in Figures S7 and S8 for dry and wet conditions, respectively, as discussed in Section 6.3.

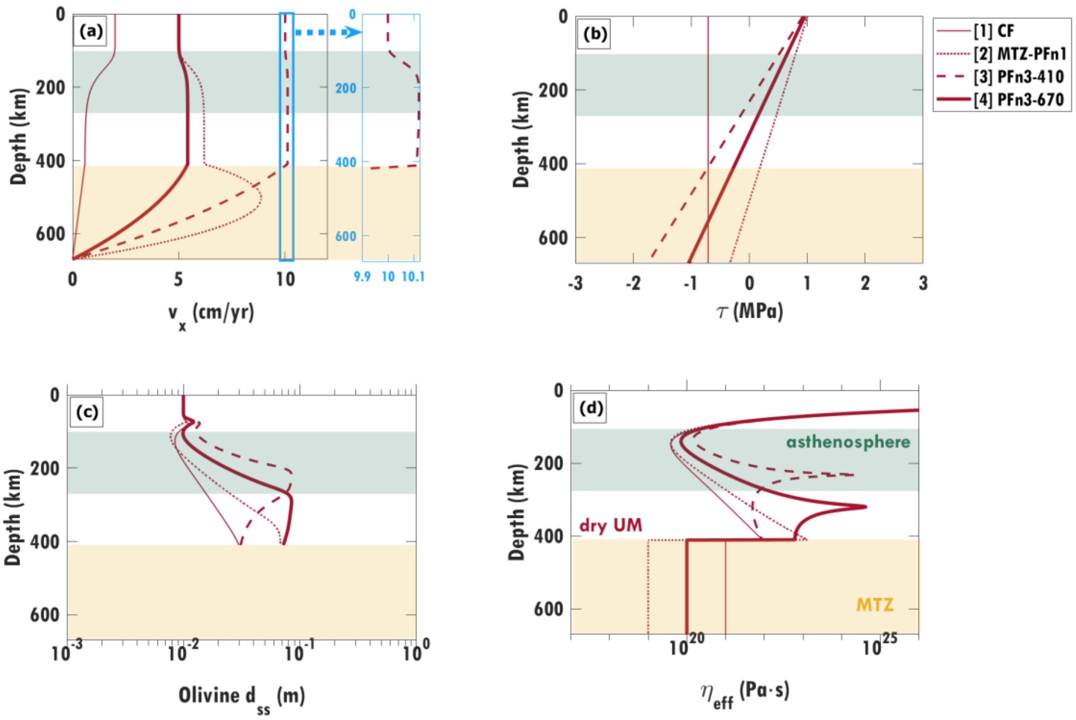

Figure S7. The (a) four flow configurations for dry (50 ppm H/Si) upper mantle and their associated (b) stresses, (c) grain-sizes, and (d) viscosity structures. The corresponding plate speed and pressure gradient combinations used to produce such flows are shown in Figure 7b.1 (in red rectangles).

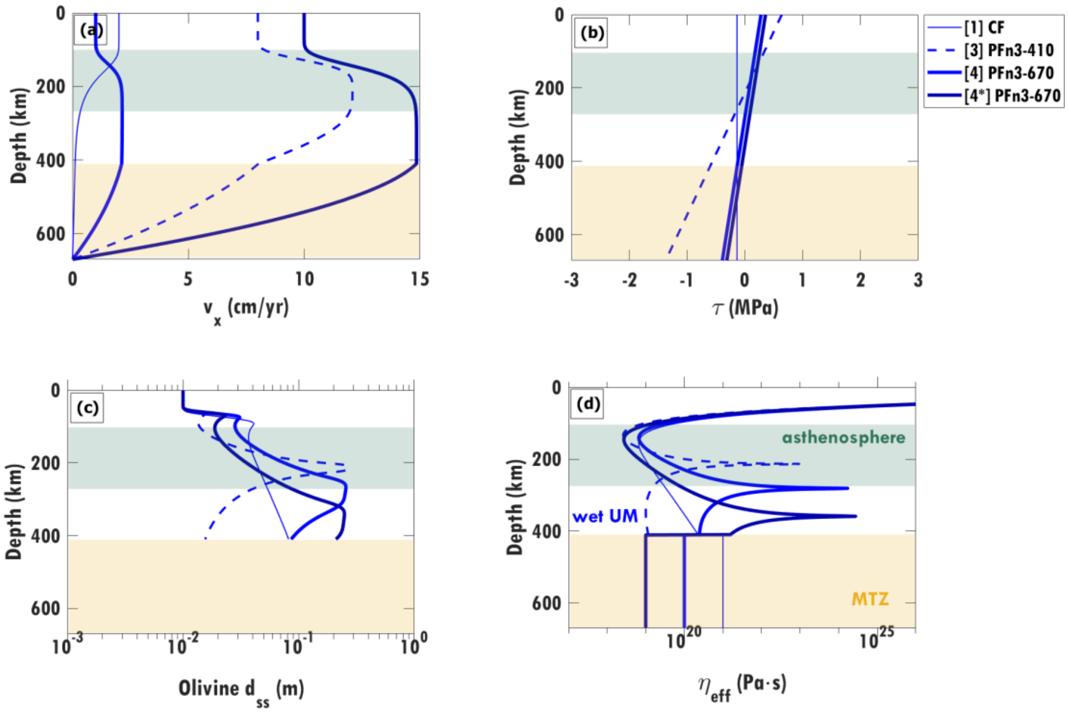

Figure S8. The (a) four flow configurations plausible for wet (1000 ppm H/Si) upper mantle and their associated (b) stresses, (c) grain-sizes, and (d) viscosity structures. The corresponding plate speed and pressure gradient combinations used to produce such flows are shown in Figure 7b.2 (in blue rectangles).